Journal of Applied Analysis and Computation
Volume 16, Number 4, August 2026, 1668–1694
Website:http://www.jaac-online.com
DOI:10.11948/20250233

HYBRID ANALYTICAL AND DYNAMICAL ANALYSIS OF A FRACTIONAL GENERALIZED DUFFING MODEL WITH ATANGANA'S CONFORMABLE DERIVATIVE

Mati ur Rahman[1] and Sonia Akram[2,†]

Abstract In this research, we analyze the fractional generalized reaction Duffing model (FGRDM) within the framework of Atangana's conformable derivative, providing a novel approach to modeling memory and hereditary characteristics in nonlinear dynamical systems. To determine exact analytical solutions, we utlize a hybrid methodology combining the Riccati sub-equation method and the Riccati–Bernoulli sub-ODE method. This integrated approach successfully yields a wide variety of soliton solutions, such as dark, bright, M-shape, combo, periodic, singular, and mixed hyperbolic wave structures. Beyond the analytical construction of solutions, we present a detailed qualitative analysis of the governed model, both in its perturbed and unperturbed forms, through bifurcation and chaos investigations. To explore the nonlinear behavior and chaotic dynamics, we employ a suite of diagnostic tools, such as Poincaré sections, return maps, Lyapunov exponents, time series analysis, power spectra, strange attractors, recurrence plots, and fractal dimension estimation. These tools help uncover the rich and sensitive dependency of the system on initial conditions and parameter variations, suggesting transitions between periodic, quasi-periodic, and chaotic regimes. The importance of this work lies in its comprehensive analytical and numerical analysis of the FGRDM using fractional calculus. It offers insights into the interplay between memory effects, nonlinearity, and chaos, thereby enhancing the comprehending of complex dynamical systems. Our research have potential applications in nonlinear science, particularly in fields where fractional-order models are used to explain physical phenomena with inherent damping and memory characteristics.

Keywords Fractional generalized reaction Duffing model, analytical approaches, exact solution, bifurcation analysis, chaos, Poincaré sections, return maps, power spectra, strange attractors, Lyapunov exponents.

MSC(2010) 35C07, 35C08, 35C09, 35G20.

1. Introduction

Nonlinear evolution equations (NLEEs) play a crucial role in the analysis and modeling of complex biological, physical, and engineering systems [9]. In contrast of linear models, NLEEs are capable of depicting essential nonlinear interactions that present the dynamics of real-world phenomena including optical pulse propagation, plasma physics, fluid flow, wave dynamics, and biological pattern formation [21,22]. Their nonlinearity often leads to intricate and rich pattern, including soliton formation, chaos, bifurcations, wave breaking, and pattern transitions [38].

[†]The corresponding author.
[1]Department of Mathematics and Statistics, College of Sciences, Imam Mohammad Ibn Saud Islamic University (IMSIU), Riyadh, Saudi Arabia
[2]Department of Mathematics, Faculty of Science, University of Gujrat, Gujrat-50700, Pakistan
Email: mrmahman@imamu.edu.sa(M. ur Rahman), soniaakram641@gmail.com(S. Akram)

These equations offer a mathematical framework to explain how systems evolve over time under the influence of both external perturbations and internal nonlinear mechanisms. The analysis of NLEEs not only contributes the development of accurate numerical methods but also facilitates to the theoretical advancement of applied mathematics, control strategies, and predictive tools in different scientific domains [39]. As such, solving and understanding NLEEs, particularly in fractional forms allows deeper insight into hereditary effects and memory-dependent that are often overlooked in classical models, thus providing more realistic and applicable solutions across distinct disciplines.

On the other hand, fractional derivatives, which generalize the concept of integer-order differentiation to arbitrary real or complex orders, have exhibited as powerful tools in the simulating of complex systems showing memory and hereditary characteristics [7, 8, 11, 34]. This makes them especially useful for capturing spatial dependencies or long-range temporal, which are common in physical, engineering, and biological phenomena [2, 26, 40]. They have proven to be significantly useful in modeling anomalous diffusion, signal processing, viscoelastic materials, control theory, epidemiology, and population dynamics [17, 25]. Among the different definitions of fractional derivatives, the Caputo and Riemann–Liouville derivatives are the most widely studied [18]. The Caputo derivative is favored in applications because it permits the use of classical initial conditions and its derivative of a constant is zero, while the Riemann–Liouville derivative is technically elegant but less appropriate for physical issues involving initial conditions [3]. For numerical applications, the Grünwald–Letnikov derivative is frequently used because it provides a discrete approximation of the Riemann–Liouville form. Other prominent forms are the Caputo–Fabrizio and Atangana–Baleanu (AB) derivatives, which introduce non-singular kernels based on exponential and Mittag-Leffler functions, respectively; the Hadamard derivative, which uses logarithmic kernels; and the Hilfer derivative, which interpolates between Riemann–Liouville and Caputo forms. These newer forms are especially suitable for systems with fading memory or non-singular stucture.

Exact solutions of NLEEs play a significant role in understanding the qualitative pattern of complex physical, engineering, and biological systems [15,31]. These solutions offer direct insight into the dynamics of stability, interaction phenomena, and wave propagation, which are often not easy to reveal through purely numerical or approximate methods. Recently, researchers have created and refined different analytical techniques to develop such solutions, especially for NLEEs and fractional-order models. These methods aim to derive soliton, kink-type, periodic, and rational solutions under certain conditions. Among the most widely used analytical techniques are the extended tanh method [28], $(\frac{G'}{G})$-expansion method [13], first integral method [5], sine-cosine method [6], Improved Kudryashov method [24], Lie symmetry analysis [23], and the modified simple equation method [12]. Additionally, a wider class of solutions has been obtained by using more advanced techniques as the Jacobi Elliptic function method [16], F-expansion method [20], and advanced projective Riccati equation method [29]. These analytical techniques not only improve our theoretical knowledge but also provide a substantial contribution to the mathematical modeling of practical systems in domains including biomathematics, fluid dynamics, plasma physics, and optical fiber communications [4, 10].

The FGRDM has gained increasing attention in recent years due to its capacity to capture intricate nonlinear dynamics inherent in different chemical, physical, and biological systems [1]. This model expands the classical Duffing equation, which explains nonlinear oscillatory systems by combining both reaction terms and fractional-order derivatives, providing a more realistic and flexible representation of memory-dependent and hereditary processes. The incorporation of fractional calculus, particularly with derivatives such as the Caputo, Riemann–Liouville, Atan-

gana–Baleanu, and Caputo–Fabrizio operators, allows the model to better capture anomalous diffusion, long-range time-dependent interactions, and viscoelastic damping all of which are frequently seen in practical applications [19].

The primary objective of this work is to construct traveling solitary wave solutions for the Fractional generalized reaction Duffing model (FGRDM) using Atangana-Baleanu derivative is defined as [27]:

$$^{\mathcal{AB}}\mathcal{D}_{2t}^{\alpha}\mathcal{M}(x,t)+\beta(\mathcal{M}(x,t))_{xx}+\gamma\mathcal{M}(x,t)+\delta^2\mathcal{M}(x,t)+\mu(\mathcal{M}(x,t))^3=0, \tag{1.1}$$

where $t>0$, $0<\alpha\leq 0$, and β, γ, δ, and μ are constants. The reaction component of the model enables for the replication of population dynamics or source sink mechanisms, making the FGRDM highly applicable in fields such as chemical kinetics, epidemiology, and biomathematics [33]. Meanwhile, the nonlinear stiffness reflected by the Duffing term models physical phenomena such as electrical circuits, optical solitons, and vibrations in mechanical systems in nonlinear media. The main motivation of this research is to construct a deeper understanding of complex nonlinear dynamics by examining the FGRDM within the framework of Atangana's conformable derivative. Traditional integer-order models often fail to capture hereditary and long-term memory effects inherent in many physical systems. By incorporating fractional calculus, especially with a non-singular and conformable operator, our work focuses to bridge this gap. Additionally, the adoption of advanced analytical approaches, namely the Riccati sub-equation and Riccati–Bernoulli sub-ODE methods, allows the derivation of diverse soliton solutions, while the combination of qualitative tools including bifurcation analysis, chaos diagnostics, and fractal measures offers a holistic exploration of the system's nature. This integrative approach is motivated by the need to model and investigate real-world systems that demonstrate both nonlinear complexity and memory-driven evolution.

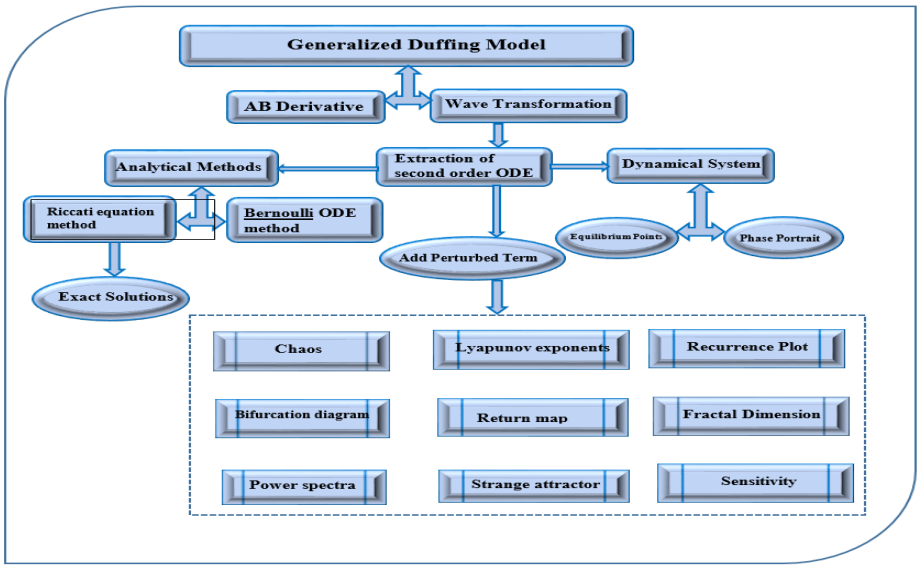

Figure 1. Graphical abstract.

Figure 1 provides the complete flowchart of the methodology and analysis applied in this study. The structure of the paper is arranged as follows. A detailed description of the chosen fractional derivative, namely the Atangana–Baleanu derivative, is presented in Section 2. In Section 3, we provide the mathematical formulation of the governed FGRDM using the logarithmic

transformation technique, along with the application of two analytical methods. Section 4 is devoted to the qualitative analysis of the model, such as bifurcation analysis, chaotic behavior, and sensitivity to initial conditions. Moreover, various graphical diagnostics, such as 2D and 3D phase portraits, Poincaré sections, and time series plots are used to visualize the system's dynamics. In Section 5, we present the physical interpretation of the derived solutions and compare various dynamical behaviors arising from the model. Finally, Section 6 concludes the paper with a summary of the main findings and potential directions for future study.

2. Description of Atangana-Baleanu derivative

The Atangana–Baleanu (AB) derivative has emerged as a key instrument in the field of fractional calculus due to its non-local and non-singular kernel, which distinguishes it from standard fractional derivatives such as the Caputo or Riemann–Liouville forms. A more realistic and accurate description of systems with long-term memory effects is made possible by the AB derivative, which was introduced to better characterize biological and physical processes with memory and hereditary qualities. Its kernel is the Mittag-Leffler function. In situations where conventional derivatives are inadequate, such as when modeling diffusion, viscoelasticity, control systems, and epidemiological dynamics, this property is quite helpful. The AB derivative has become a crucial part of contemporary mathematical modeling, providing a link between theoretical advancement and practical applications in complex systems while preserving the model's physical interpretability and guaranteeing improved numerical stability and smoother analytical behavior.

Definition 2.1. The valuable definition of a new conformable derivative has been characterized in [30] as:

$$ {}_0^{\mathcal{AB}}\mathcal{D}_t^{\alpha}\{\mathcal{T}(t)\} = \lim_{\varpi\to 0} \frac{\mathcal{T}(t+\varpi t^{1-\alpha}) - \mathcal{T}(t)}{\varpi},\ \mathcal{T} := [0,\infty),\ t>0,\ \alpha\in(0,1). \tag{2.1} $$

Definition 2.2. The valuable definition of the ABD has been characterized in as:

$$ {}_0^{\mathcal{AB}}\mathcal{D}_t^{\alpha}\{\mathcal{T}(t)\} = \lim_{\varpi\to 0} \frac{\mathcal{T}\left((t+\varpi\left(t+\frac{1}{\Gamma(\alpha)}\right)^{1-\alpha}\right) - \mathcal{T}(t)}{\varpi}. \tag{2.2} $$

The properties of the ABD are taken as:

$$ \begin{cases} {}_0^{\mathcal{AB}}\mathcal{D}_t^{\alpha}\{\mathcal{P}\mathcal{G}(x)+\mathcal{Q}\mathcal{H}(x)\} = \mathcal{P}\,{}_0^{\mathcal{AB}}\mathcal{D}_x^{\alpha}\{\mathcal{G}(x)\} + \mathcal{Q}\,{}_0^{\mathcal{AB}}\mathcal{D}_x^{\alpha}\{\mathcal{H}(x)\},\ \mathcal{P},\mathcal{Q}\in\Re,\ \mathcal{H}\neq 0,\\ {}_0^{\mathcal{AB}}\mathcal{D}_x^{\alpha}\{\mathcal{P}\} = 0,\\ {}_0^{\mathcal{AB}}\mathcal{D}_x^{\alpha}\{\mathcal{G}(x)\mathcal{H}(x)\} = \mathcal{H}(x)\,{}_0^{\mathcal{AB}}\mathcal{D}_x^{\alpha}\{\mathcal{G}(x)\} + \mathcal{G}(x)\,{}_0^{\mathcal{AB}}\mathcal{D}_x^{\alpha}\{\mathcal{H}(x)\},\\ {}_0^{\mathcal{AB}}\mathcal{D}_x^{\alpha}\{\frac{\mathcal{G}(x)}{\mathcal{H}(x)}\} = \frac{\mathcal{H}(x)\,{}_0^{\mathcal{AB}}\mathcal{D}_x^{\alpha}\{\mathcal{G}(x)\} - \mathcal{G}(x)\,{}_0^{\mathcal{AB}}\mathcal{D}_x^{\alpha}\{\mathcal{H}(x)\}}{\mathcal{H}^2(x)},\\ \varpi = \left(x+\frac{1}{\Gamma(\alpha)}\right)^{\alpha-1}\mathcal{H},\\ {}_0^{\mathcal{AB}}\mathcal{D}_x^{\alpha}\{\mathcal{H}\} = \left(x+\frac{1}{\Gamma(\alpha)}\right)^{1-\alpha}\frac{d\mathcal{H}(x)}{dx},\\ {}_0^{\mathcal{AB}}\mathcal{D}_x^{\alpha}\{\mathcal{H}(x)\} = \mathcal{P}_1\frac{d\mathcal{H}(\varpi)}{d(\eta)} \text{ with } \varpi = \frac{\mathcal{P}_1}{\alpha}\left(x+\frac{1}{\Gamma(\alpha)}\right)^{\alpha}. \end{cases} \tag{2.3} $$

2.1. Mathematical formulation of the methods

This section will provide a description of the methods used. We look at a specific kind of fractional equation that is not linear

$$\mathscr{E}\left(\boldsymbol{\mathcal{M}},\ {}_{0}^{\mathcal{AB}}\boldsymbol{\mathcal{D}}_{t}^{\alpha}\{\boldsymbol{\mathcal{M}}\},\ {}_{0}^{\mathcal{AB}}\boldsymbol{\mathcal{D}}_{t}^{2\alpha}\{\boldsymbol{\mathcal{M}}\},\ \{\boldsymbol{\mathcal{M}}\}_{x},\ \{\boldsymbol{\mathcal{M}}\}_{xx},\ \cdots\right)=0. \tag{2.4}$$

The wave transformation is described as:

$$\boldsymbol{\mathcal{M}}(x,t)=\boldsymbol{\mathcal{N}}(\varpi),\quad \text{where}\ \ \varpi=(\delta x+\frac{\kappa(1-\delta)t^{-p}}{\boldsymbol{\mathcal{W}}(\alpha)\sum_{p=0}^{\infty}\left(-\frac{\alpha}{1-\alpha}\right)^{p}\Gamma(1-\alpha p)}). \tag{2.5}$$

Here, the amplitude is shown by $\boldsymbol{\mathcal{N}}(\varpi)$. Eq. (2.5) is transformed into a nonlinear ordinary differential equation (ODE) in accordance with the strategy:

$$\mathscr{F}(\boldsymbol{\mathcal{N}},\ \boldsymbol{\mathcal{N}}',\ \boldsymbol{\mathcal{N}}'',\ \ \boldsymbol{\mathcal{N}}''',\ \cdots)=0. \tag{2.6}$$

2.2. Algorithm of Riccati sub-equation method

In this section, we describe the steps involved in Riccati sub-equation method. Following steps are involved

Step 1. Assume the following is the trial solution of Eq. (2.6) to obtain different results:

$$\boldsymbol{\mathcal{N}}(\varpi)=\boldsymbol{\mathcal{D}}_{0}+\sum_{i=1}^{n}\boldsymbol{\mathcal{D}}_{i}\boldsymbol{\mathcal{R}}(\varpi)^{i},\ \boldsymbol{\mathcal{D}}_{n}\neq 0. \tag{2.7}$$

Where $\boldsymbol{\mathcal{D}}_{i}(i=0,1,2,\cdots,n)$ re unknown constants. Besides, $\boldsymbol{\mathcal{D}}(\varpi)$ obeys the following Ricati equation:

$$(\boldsymbol{\mathcal{R}}'(\varpi))^{2}=\sigma+\boldsymbol{\mathcal{R}}^{2}(\varpi), \tag{2.8}$$

where σ is a constant. In order to find the general solutions of (2.8) by Riccati sub-equation method, we are able to arrive at the following expression:

Type 1: When $\sigma<0$.

$$\begin{cases}
\boldsymbol{\mathcal{R}}_{1}(x,t)=\sqrt{-\sigma}\tanh_{pq}\left(\varpi\sqrt{-\sigma}\right),\\
\boldsymbol{\mathcal{R}}_{2}(x,t)=\sqrt{-\sigma}\coth_{pq}\left(\varpi\sqrt{-\sigma}\right),\\
\boldsymbol{\mathcal{R}}_{3}(x,t)=\sqrt{-\sigma}\left(\tanh_{pq}\left(2\varpi\sqrt{-\sigma}\right)\pm i\sqrt{-\sigma}\mathrm{sech}_{pq}\left(\varpi\sqrt{-\sigma}\right)\right),\\
\boldsymbol{\mathcal{R}}_{4}(x,t)=\sqrt{-\sigma}\left(\coth_{pq}\left(2\varpi\sqrt{-\sigma}\right)\pm\sqrt{-\sigma}\mathrm{csch}_{pq}\left(2\varpi\sqrt{-\sigma}\right)\right),\\
\boldsymbol{\mathcal{R}}_{5}(x,t)=-\frac{1}{2}\left(\sqrt{-\sigma}\tanh_{pq}\left(\frac{\varpi\sqrt{-\sigma}}{2}\right)+\sqrt{-\sigma}\coth_{pq}\left(\frac{\varpi\sqrt{-\sigma}}{2}\right)\right),\\
\boldsymbol{\mathcal{R}}_{6}(x,t)=-\dfrac{\sqrt{\sigma\left(-(Q^{2}+S^{2})\right)}-Q\sqrt{-\sigma}\cosh_{pq}\left(2\varpi\sqrt{-\sigma}\right)}{2\left(Q\sinh_{pq}\left(2\varpi\sqrt{-\sigma}\right)+S\right)},\\
\boldsymbol{\mathcal{R}}_{1}(x,t)=-\dfrac{\sqrt{\sigma\left(-(Q^{2}+S^{2})\right)}-Q\sqrt{-\sigma}\sinh_{pq}\left(2\varpi\sqrt{-\sigma}\right)}{2\left(Q\cosh_{pq}\left(2\varpi\sqrt{-\sigma}\right)+S\right)},
\end{cases} \tag{2.9}$$

where Q and S are two non-zero real constants and $S^2 - Q^2 > 0$.

Type 2: When $\sigma > 0$

$$\begin{cases} \boldsymbol{\mathcal{R}}_8(x,t) = \sqrt{\sigma}\tan_{pq}\left(\varpi\sqrt{-\sigma}\right), \\ \boldsymbol{\mathcal{R}}_9(x,t) = -\sqrt{\sigma}\cot_{pq}\left(\varpi\sqrt{-\sigma}\right), \\ \boldsymbol{\mathcal{R}}_{10}(x,t) = -\sqrt{\sigma}\left(\tan_{pq}\left(2\varpi\sqrt{\sigma}\right) \pm \sqrt{\sigma}\sec_{pq}\left(2\varpi\sqrt{\sigma}\right)\right), \\ \boldsymbol{\mathcal{R}}_{11}(x,t) = -\sqrt{\sigma}\left(\cot_{pq}\left(2\varpi\sqrt{\sigma}\right) \pm \sqrt{\sigma}\csc_{pq}\left(2\varpi\sqrt{\sigma}\right)\right), \\ \boldsymbol{\mathcal{R}}_{12}(x,t) = \dfrac{1}{2}\left(\sqrt{\sigma}\tan_{pq}\left(\dfrac{\varpi\sqrt{\sigma}}{2}\right) - \sqrt{\sigma}\cot_{pq}\left(\dfrac{\varpi\sqrt{\sigma}}{2}\right)\right), \\ \boldsymbol{\mathcal{R}}_{13}(x,t) = \dfrac{\pm\sqrt{\sigma\left((Q^2+S^2)\right)} - Q\sqrt{-\sigma}\cos_{pq}\left(2\varpi\sqrt{\sigma}\right)}{2\left(Q\sin_{pq}\left(2\varpi\sqrt{\sigma}\right)+S\right)}, \\ \boldsymbol{\mathcal{R}}_{14}(x,t) = \dfrac{\pm\sqrt{\sigma\left((Q^2+S^2)\right)} - Q\sqrt{\sigma}\sin_{pq}\left(2\varpi\sqrt{\sigma}\right)}{2\left(Q\cos_{pq}\left(2\varpi\sqrt{\sigma}\right)+S\right)}, \end{cases} \tag{2.10}$$

where Q and S are two non-zero real constants and $Q^2 - R^2 > 0$.

Type 3: When $\sigma = 0$

$$\boldsymbol{\mathcal{R}}_{15}(x,t) = -\frac{1}{\varpi + h}. \tag{2.11}$$

The definitions of generalized hyperbolic functions are

$$\begin{cases} \sinh_{pq}(\varpi) = \dfrac{pe^{\varpi} - qe^{-\varpi}}{2}, \ \cosh_{pq}(\varpi) = \dfrac{pe^{\varpi} + qe^{-\varpi}}{2}, \ \tanh_{pq}(\varpi) = \dfrac{pe^{\varpi} - qe^{-\varpi}}{pe^{\varpi} + qe^{-\varpi}}, \\ \operatorname{csch}_{pq}(\varpi) = \dfrac{2}{pe^{\varpi} - qe^{-\varpi}}, \ \operatorname{sech}_{pq}(\varpi) = \dfrac{2}{pe^{\varpi} + qe^{-\varpi}}, \ \coth_{pq}(\varpi) = \dfrac{pe^{\varpi} + qe^{-\varpi}}{pe^{\varpi} - qe^{-\varpi}}, \end{cases} \tag{2.12}$$

where p and q are positive constants.

Moreover, generalized triangular functions are defined as the aforementioned six different types of functions, where p and q are positive constants, called deformation parameters:

$$\begin{cases} \sin_{pq}(\varpi) = \dfrac{pe^{i\varpi} - qe^{-i\varpi}}{2}, \ \cos_{pq}(\varpi) = \dfrac{pe^{i\varpi} + qe^{-i\varpi}}{2}, \ \tan_{pq}(\varpi) = -i\dfrac{pe^{i\varpi} - qe^{-i\varpi}}{pe^{\varpi} + qe^{-i\varpi}}, \\ \csc_{pq}(\varpi) = \dfrac{2}{pe^{i\varpi} - qe^{-i\varpi}}, \ \operatorname{sech}_{pq}(\varpi) = \dfrac{2}{pe^{i\varpi} + qe^{-i\varpi}}, \ \cot_{pq}(\varpi) = i\dfrac{pe^{i\varpi} + qe^{-i\varpi}}{pe^{i\varpi} - qe^{-i\varpi}}. \end{cases} \tag{2.13}$$

Step 2. Using the balance theory on Eq. (2.6), we determine the value of N.

Step 3. Eqs. (2.7) and (2.8) are switched into Eq. (2.6), and all of the coefficients of power of $\boldsymbol{\mathcal{R}}(\varpi)$ are set to zero. In order to obtain the values of the unknowns $\boldsymbol{\mathcal{D}}_0$, $\boldsymbol{\mathcal{D}}_i$, and σ, which will be used to derive the solution of Eq. (2.4), we finally solve these equations using the computation program.

2.3. The Riccati-Bernoulli sub-ODE method scheme

The Riccati-Bernoulli sub-ODE method is a powerful analytical technique designed to create exact solutions for NLEEs. Numerous scientific disciplines, such as engineering, physics, and

applied mathematics, commonly use these equations to describe complex phenomena. The basic steps of this technique is provided below.

Step 1. Assume that Eq. (2.6) has the following trial solution:

$$\boldsymbol{\mathcal{N}}(\varpi) = \boldsymbol{\mathcal{C}}_0 + \sum_{i=0}^{n} \boldsymbol{\mathcal{C}}_i \boldsymbol{\mathcal{B}}(\varpi)^i, \tag{2.14}$$

$$\boldsymbol{\mathcal{B}}(\varpi) = \frac{-\mathfrak{F} b + a\boldsymbol{\mathcal{B}}(\varpi)}{a + b\boldsymbol{\mathcal{B}}(\varpi)}, \tag{2.15}$$

with constants $\mathfrak{F},\ a$, and b, suppose that $b \neq 0$ and introduce the function $\boldsymbol{\mathcal{B}}(\varpi)$ provided as:

$$\frac{d\boldsymbol{\mathcal{B}}}{d\varpi} = \mathfrak{F} + \boldsymbol{\mathcal{B}}^2(\varpi). \tag{2.16}$$

The value of $\mathfrak{F}$ is then used to deduce the following analyses and the solution $\boldsymbol{\mathcal{B}}(\varpi)$ to be obtained.

Type 1: When $\mathfrak{F} < 0$, then

$$\begin{cases} \boldsymbol{\mathcal{B}}_1(\varpi) = -\sqrt{-\mathfrak{F}} \tanh(\sqrt{-\mathfrak{F}}\varpi), \\ \boldsymbol{\mathcal{B}}_2(\varpi) = -\sqrt{-\mathfrak{F}} \coth(\sqrt{-\mathfrak{F}}\varpi). \end{cases} \tag{2.17}$$

Type 2: When $\mathfrak{F} > 0$, then

$$\begin{cases} \boldsymbol{\mathcal{B}}_3(\varpi) = \sqrt{\mathfrak{F}} \tan(\sqrt{\mathfrak{F}}\varpi), \\ \boldsymbol{\mathcal{B}}_4(\varpi) = -\sqrt{\mathfrak{F}} \cot(\sqrt{\mathfrak{F}}\varpi). \end{cases} \tag{2.18}$$

Type 3: When $\mathfrak{F} = 0$, then

$$\boldsymbol{\mathcal{B}}_5(\varpi) = -\frac{1}{\varpi}. \tag{2.19}$$

Step 2. By using the balance theory on Eq. (2.7), we get the value of n.

Step 3. Eqs. (2.15) and (2.16) are switched into Eq. (2.6), and all of the coefficients of power of $\boldsymbol{\mathcal{B}}(\varpi)$ are set to zero. In order to obtain the values of the unknowns $\boldsymbol{\mathcal{C}}_0,\ \boldsymbol{\mathcal{C}}_i,\ a$, and b, which will be used to determine the solution of Eq. (2.4), we finally solve these equations using the computation program.

3. Extaction of exact solutions

In this section, we apply the two hybrid analytical method to Eq. (1.1) in order to determine the required solutions. So first, we convert Eq. (1.1) to an ODE using appropriate wave transformation as:

$$\boldsymbol{\mathcal{M}}(x,t) = \boldsymbol{\mathcal{N}}(\varpi), \quad \text{where } \varpi = (\delta x + \frac{\kappa(1-\delta)t^{-p}}{\boldsymbol{\mathcal{W}}(\alpha)\sum_{p=0}^{\infty}\left(-\frac{\alpha}{1-\alpha}\right)^p \Gamma(1-\alpha p)}), \tag{3.1}$$

where $\delta,\ \kappa$, represent wave number, and velocity of the soliton, respectively. The wave transformations in Eq. (3.1) are employed to reduce the fractional PDEs into a more tractable form

by introducing a traveling wave coordinate, κ, which characterizes the soliton dynamics within a moving reference frame. From a physical perspective, this approach facilitates the description of solitary wave propagation in a nonlinear medium exhibiting memory effects. In nonlinear wave theory, such transformations align with classical analytical techniques and are particularly effective for systems governed by fractional derivatives [35,36]. Putting Eq. (3.1) into Eq. (1.1), we get

$$\kappa^2 \boldsymbol{\mathcal{N}}'' + \beta\delta^2 \boldsymbol{\mathcal{N}}'' + \gamma \boldsymbol{\mathcal{N}} + \mu \boldsymbol{\mathcal{N}}^3 = 0. \tag{3.2}$$

A detailed description of the balancing process for Eq. (3.2) is included here to clarify the second step of the adopted technique. Following the homogeneous balance principle [37], the degrees of the highest-order derivative term and the dominant nonlinear term must be equal to ensure a consistent analytical form of the assumed solution.

Let the degree of $\boldsymbol{\mathcal{N}}(\varpi)$ be denoted by n, i.e., $\deg[\boldsymbol{\mathcal{N}}(\varpi)] = n$. According to the general rule, the degree of the k-th derivative of $\boldsymbol{\mathcal{N}}(\varpi)$ is $\deg[\boldsymbol{\mathcal{N}}^{(k)}(\eta)] = n + k$. For the second derivative ($k = 2$), we obtain $\deg[\boldsymbol{\mathcal{N}}''(\varpi)] = n + 2$. The degree of a power term is given by $\deg[(\boldsymbol{\mathcal{N}}(\varpi))^p] = pn$; therefore, for the cubic term ($p = 3$), $\deg[\boldsymbol{\mathcal{N}}^3(\varpi)] = 3n$.

By applying the balance condition between the highest-order linear and nonlinear terms, we have

$$\deg[\boldsymbol{\mathcal{N}}''(\varpi)] = \deg[\boldsymbol{\mathcal{N}}^3(\varpi)].$$

Substituting the corresponding degrees gives

$$n + 2 = 3n,$$

which yields the integer value

$$n = 1.$$

This balancing relation ensures that the constructed solution ansatz properly represents the interaction between the linear and nonlinear components of the governing equation.

3.1. Riccati sub-equation method

By balancing the heights order nonlinear terms with the derivatives in Eq. (3.2), we obtain $n = 1$. Then, from Eq. (2.7), the general solutions of Eq. (3.2) are as:

$$\boldsymbol{\mathcal{N}}(\varpi) = \boldsymbol{\mathcal{C}}_0 + \boldsymbol{\mathcal{C}}_1 \boldsymbol{\mathcal{R}}(\varpi). \tag{3.3}$$

Eq. (3.3) is plugged into Eq. (3.2) using Eq. (2.8), yielding the polynomial in a different power of $\boldsymbol{\mathcal{R}}(\varpi)$. A system of algebraic equations can be obtained by collecting each term with the same exponent of $\boldsymbol{\mathcal{R}}^k(\varpi)$, $(k = 0, \pm1, \pm2, \pm3)$, and setting each coefficient to zero. Numerous solution sets are produced after these systems of equations are solved, but we only utilize the sets that we used for the graphical analysis. The above system's solution sets can be written as follows:

$$\begin{cases} Set^1 \ \boldsymbol{\mathcal{C}}_0 = 0, \ \boldsymbol{\mathcal{C}}_1 = \dfrac{\sqrt{2}\sqrt{-\beta\delta^2 - \kappa^2}}{\sqrt{\mu}}, \ \gamma = -2\sigma\left(\beta\delta^2 + \kappa^2\right), \ \kappa = \kappa, \ \delta = \delta, \\ Set^2 \ \boldsymbol{\mathcal{C}}_0 = 0, \ \boldsymbol{\mathcal{C}}_1 = -\dfrac{\sqrt{\gamma}}{\sqrt{\mu}\sqrt{\sigma}}, \ \kappa = \dfrac{\sqrt{-2\beta\delta^2\sigma - \gamma}}{\sqrt{2}\sqrt{\sigma}}, \ \delta = \delta, \\ Set^3 \ \boldsymbol{\mathcal{C}}_0 = 0, \ \boldsymbol{\mathcal{C}}_1 = \dfrac{\sqrt{\gamma}}{\sqrt{\mu}\sqrt{\sigma}}, \delta = \dfrac{\sqrt{-\gamma - 2\kappa^2\sigma}}{\sqrt{2}\sqrt{\beta}\sqrt{\sigma}}, \ \kappa = \kappa. \end{cases} \tag{3.4}$$

Here, we consider first set to retrieve the solutions of Eq. (1.1):

Type 1: When $\sigma < 0$.

$$\boldsymbol{\mathcal{M}}_1(x,t) = \left[\frac{\sqrt{2}\sqrt{-\sigma}\sqrt{-\beta\delta^2-\kappa^2}\tanh\left((\delta x+\frac{\kappa(1-\delta)t^{-p}}{\boldsymbol{\mathcal{W}}(\alpha)\sum_{p=0}^{\infty}\left(-\frac{\alpha}{1-\alpha}\right)^p\Gamma(1-\alpha p)})\sqrt{-\sigma}\right)}{\sqrt{\mu}}\right], \tag{3.5}$$

$$\boldsymbol{\mathcal{M}}_2(x,t) = \left[\frac{\sqrt{2}\sqrt{-\sigma}\sqrt{-\beta\delta^2-\kappa^2}\coth\left((\delta x+\frac{\kappa(1-\delta)t^{-p}}{\boldsymbol{\mathcal{W}}(\alpha)\sum_{p=0}^{\infty}\left(-\frac{\alpha}{1-\alpha}\right)^p\Gamma(1-\alpha p)})\sqrt{-\sigma}\right)}{\sqrt{\mu}}\right], \tag{3.6}$$

$$\boldsymbol{\mathcal{M}}_3(x,t) = \left[\frac{\sqrt{2}\sqrt{-\sigma}\sqrt{-\beta\delta^2-\kappa^2}\left(\tanh\left(2(\delta x+\frac{\kappa(1-\delta)t^{-p}}{\boldsymbol{\mathcal{W}}(\alpha)\sum_{p=0}^{\infty}\left(-\frac{\alpha}{1-\alpha}\right)^p\Gamma(1-\alpha p)})\sqrt{-\sigma}\right)+i\sqrt{-\sigma}\operatorname{sech}\left((\delta x+\frac{\kappa(1-\delta)t^{-p}}{\boldsymbol{\mathcal{W}}(\alpha)\sum_{p=0}^{\infty}\left(-\frac{\alpha}{1-\alpha}\right)^p\Gamma(1-\alpha p)})\sqrt{-\sigma}\right)\right)}{\sqrt{\mu}}\right], \tag{3.7}$$

$$\boldsymbol{\mathcal{M}}_4(x,t) = \left[\frac{\sqrt{2}\sqrt{-\sigma}\sqrt{-\beta\delta^2-\kappa^2}\left(\cosh\left(2(\delta x+\frac{\kappa(1-\delta)t^{-p}}{\boldsymbol{\mathcal{W}}(\alpha)\sum_{p=0}^{\infty}\left(-\frac{\alpha}{1-\alpha}\right)^p\Gamma(1-\alpha p)})\sqrt{-\sigma}\right)+\sqrt{-\sigma}\right)\operatorname{csch}\left(2(\delta x+\frac{\kappa(1-\delta)t^{-p}}{\boldsymbol{\mathcal{W}}(\alpha)\sum_{p=0}^{\infty}\left(-\frac{\alpha}{1-\alpha}\right)^p\Gamma(1-\alpha p)})\sqrt{-\sigma}\right)}{\sqrt{\mu}}\right], \tag{3.8}$$

$$\boldsymbol{\mathcal{M}}_5(x,t) = \left[\frac{\sqrt{-\beta\delta^2-\kappa^2}\left(\sqrt{-\sigma}\left(-\tanh\left(\frac{(\delta x+\frac{\kappa(1-\delta)t^{-p}}{\boldsymbol{\mathcal{W}}(\alpha)\sum_{p=0}^{\infty}\left(-\frac{\alpha}{1-\alpha}\right)^p\Gamma(1-\alpha p)})\sqrt{-\sigma}}{2}\right)\right)+\left(-\sqrt{-\sigma}\right)\coth\left(\frac{(\delta x+\frac{\kappa(1-\delta)t^{-p}}{\boldsymbol{\mathcal{W}}(\alpha)\sum_{p=0}^{\infty}\left(-\frac{\alpha}{1-\alpha}\right)^p\Gamma(1-\alpha p)})\sqrt{-\sigma}}{2}\right)\right)}{\sqrt{2}\sqrt{\mu}}\right], \tag{3.9}$$

$$\boldsymbol{\mathcal{M}}_6(x,t) = \left[\frac{\sqrt{-\beta\delta^2-\kappa^2}\left(Q\sqrt{-\sigma}\cosh\left(2(\delta x+\frac{\kappa(1-\delta)t^{-p}}{\boldsymbol{\mathcal{W}}(\alpha)\sum_{p=0}^{\infty}\left(-\frac{\alpha}{1-\alpha}\right)^p\Gamma(1-\alpha p)})\sqrt{-\sigma}\right)-\sqrt{-(\sigma(Q^2+S^2))}\right)}{\sqrt{2}\sqrt{\mu}\left(Q\sinh\left(2(\delta x+\frac{\kappa(1-\delta)t^{-p}}{\boldsymbol{\mathcal{W}}(\alpha)\sum_{p=0}^{\infty}\left(-\frac{\alpha}{1-\alpha}\right)^p\Gamma(1-\alpha p)})\sqrt{-\sigma}\right)+S\right)}\right], \tag{3.10}$$

$$\boldsymbol{\mathcal{M}}_7(x,t) = \left[\frac{\sqrt{-\beta\delta^2-\kappa^2}\left(Q\sqrt{-\sigma}\sinh\left(2(\delta x+\frac{\kappa(1-\delta)t^{-p}}{\boldsymbol{\mathcal{W}}(\alpha)\sum_{p=0}^{\infty}\left(-\frac{\alpha}{1-\alpha}\right)^p\Gamma(1-\alpha p)})\sqrt{-\sigma}\right)-\sqrt{-(\sigma(Q^2+S^2))}\right)}{\sqrt{2}\sqrt{\mu}\left(Q\cosh\left(2(\delta x+\frac{\kappa(1-\delta)t^{-p}}{\boldsymbol{\mathcal{W}}(\alpha)\sum_{p=0}^{\infty}\left(-\frac{\alpha}{1-\alpha}\right)^p\Gamma(1-\alpha p)})\sqrt{-\sigma}\right)+S\right)}\right]. \tag{3.11}$$

Type 2: When $\sigma > 0$, then

$$\boldsymbol{\mathcal{M}}_8(x,t) = \left[\frac{\sqrt{2}\sqrt{\sigma}\sqrt{-\beta\delta^2-\kappa^2}\tan\left((\delta x+\frac{\kappa(1-\delta)t^{-p}}{\boldsymbol{\mathcal{W}}(\alpha)\sum_{p=0}^{\infty}\left(-\frac{\alpha}{1-\alpha}\right)^p\Gamma(1-\alpha p)})\sqrt{\sigma}\right)}{\sqrt{\mu}}\right], \tag{3.12}$$

$$\boldsymbol{\mathcal{M}}_9(x,t) = \left[-\frac{\sqrt{2}\sqrt{\sigma}\sqrt{-\beta\delta^2-\kappa^2}\cot\left((\delta x+\frac{\kappa(1-\delta)t^{-p}}{\boldsymbol{\mathcal{W}}(\alpha)\sum_{p=0}^{\infty}\left(-\frac{\alpha}{1-\alpha}\right)^p\Gamma(1-\alpha p)})\sqrt{\sigma}\right)}{\sqrt{\mu}}\right], \tag{3.13}$$

$$\boldsymbol{\mathcal{M}}_{10}(x,t) = \left[\frac{\sqrt{2}\sqrt{\sigma}\sqrt{-\beta\delta^2-\kappa^2}\left(\sec\left(2(\delta x+\frac{\kappa(1-\delta)t^{-p}}{\boldsymbol{\mathcal{W}}(\alpha)\sum_{p=0}^{\infty}\left(-\frac{\alpha}{1-\alpha}\right)^p\Gamma(1-\alpha p)})\sqrt{\sigma}\right)-\tan\left(2(\delta x+\frac{\kappa(1-\delta)t^{-p}}{\boldsymbol{\mathcal{W}}(\alpha)\sum_{p=0}^{\infty}\left(-\frac{\alpha}{1-\alpha}\right)^p\Gamma(1-\alpha p)})\sqrt{\sigma}\right)\right)}{\sqrt{\mu}}\right], \tag{3.14}$$

$$\boldsymbol{\mathcal{M}}_{11}(x,t) = \left[\frac{\sqrt{2}\sqrt{-\beta\delta^2-\kappa^2}\left(\sqrt{\sigma}\csc\left(2(\delta x+\frac{\kappa(1-\delta)t^{-p}}{\boldsymbol{\mathcal{W}}(\alpha)\sum_{p=0}^{\infty}\left(-\frac{\alpha}{1-\alpha}\right)^p\Gamma(1-\alpha p)})\sqrt{\sigma}\right)-\sqrt{\sigma}\cot\left(2(\delta x+\frac{\kappa(1-\delta)t^{-p}}{\boldsymbol{\mathcal{W}}(\alpha)\sum_{p=0}^{\infty}\left(-\frac{\alpha}{1-\alpha}\right)^p\Gamma(1-\alpha p)})\sqrt{\sigma}\right)\right)}{\sqrt{\mu}}\right], \tag{3.15}$$

$$\boldsymbol{\mathcal{M}}_{12}(x,t)=\left[\frac{\sqrt{-\beta\delta^2-\kappa^2}\left(\sqrt{\sigma}\tan\left(\frac{(\delta x+\frac{\kappa(1-\delta)t^{-p}}{\boldsymbol{\mathcal{W}}(\alpha)\sum_{p=0}^{\infty}\left(-\frac{\alpha}{1-\alpha}\right)^{p}\Gamma(1-\alpha p)})\sqrt{\sigma}}{2}\right)-\sqrt{\sigma}\cot\left(\frac{(\delta x+\frac{\kappa(1-\delta)t^{-p}}{\boldsymbol{\mathcal{W}}(\alpha)\sum_{p=0}^{\infty}\left(-\frac{\alpha}{1-\alpha}\right)^{p}\Gamma(1-\alpha p)})\sqrt{\sigma}}{2}\right)\right)}{\sqrt{2}\sqrt{\mu}}\right], \tag{3.16}$$

$$\boldsymbol{\mathcal{M}}_{13}(x,t)=\left[\frac{\sqrt{2}\sqrt{-\beta\delta^2-\kappa^2}\left(\sqrt{\sigma(Q^2-S^2)}-Q\sqrt{\sigma}\cos\left(2(\delta x+\frac{\kappa(1-\delta)t^{-p}}{\boldsymbol{\mathcal{W}}(\alpha)\sum_{p=0}^{\infty}\left(-\frac{\alpha}{1-\alpha}\right)^{p}\Gamma(1-\alpha p)})\sqrt{\sigma}\right)\right)}{\sqrt{\mu}\left(Q\sinh\left(2(\delta x+\frac{\kappa(1-\delta)t^{-p}}{\boldsymbol{\mathcal{W}}(\alpha)\sum_{p=0}^{\infty}\left(-\frac{\alpha}{1-\alpha}\right)^{p}\Gamma(1-\alpha p)})\sqrt{\sigma}\right)+S\right)}\right], \tag{3.17}$$

$$\boldsymbol{\mathcal{M}}_{14}(x,t)=\left[\frac{\sqrt{2}\sqrt{-\beta\delta^2-\kappa^2}\left(\sqrt{\sigma(Q^2-S^2)}-Q\sqrt{\sigma}\sin\left(2(\delta x+\frac{\kappa(1-\delta)t^{-p}}{\boldsymbol{\mathcal{W}}(\alpha)\sum_{p=0}^{\infty}\left(-\frac{\alpha}{1-\alpha}\right)^{p}\Gamma(1-\alpha p)})\sqrt{\sigma}\right)\right)}{\sqrt{\mu}\left(Q\cos\left(2(\delta x+\frac{\kappa(1-\delta)t^{-p}}{\boldsymbol{\mathcal{W}}(\alpha)\sum_{p=0}^{\infty}\left(-\frac{\alpha}{1-\alpha}\right)^{p}\Gamma(1-\alpha p)})\sqrt{\sigma}\right)+S\right)}\right]. \tag{3.18}$$

Type 3: When $\sigma=0$, then

$$\boldsymbol{\mathcal{M}}_{15}(x,t)=\left[\frac{\sqrt{2}\sqrt{-\beta\delta^2-\kappa^2}}{\sqrt{\mu}((\delta x+\frac{\kappa(1-\delta)t^{-p}}{\boldsymbol{\mathcal{W}}(\alpha)\sum_{p=0}^{\infty}\left(-\frac{\alpha}{1-\alpha}\right)^{p}\Gamma(1-\alpha p)})+h)}\right]. \tag{3.19}$$

3.2. Riccati-Bernoulli sub-ODE method

According to the Riccati-Bernoulli sub-ODE method, from Eq. (2.15)

$$\boldsymbol{\mathcal{N}}(\varpi)=\boldsymbol{\mathcal{C}}_0+\boldsymbol{\mathcal{C}}_1\boldsymbol{\mathcal{B}}(\varpi)+\boldsymbol{\mathcal{C}}_{-1}\boldsymbol{\mathcal{B}}(\varpi)^{-1}, \tag{3.20}$$

by merging Eq. (3.20) and Eq. (2.16) in Eq. (3.2) and we get solution sets:

$$\begin{cases}\text{Set}^1:\ \boldsymbol{\mathcal{C}}_0=0,\ \boldsymbol{\mathcal{C}}_1=\boldsymbol{\mathcal{C}}_1,\ \boldsymbol{\mathcal{C}}_{-1}=\boldsymbol{\mathcal{C}}_1\mathfrak{F},\ \delta=\dfrac{\sqrt{-c_1^2\mu-2\kappa^2}}{\sqrt{2}\sqrt{\beta}},\ \gamma=-2c_1^2\mu\mathfrak{F},\\ \text{Set}^2:\ \boldsymbol{\mathcal{C}}_0=0,\ \boldsymbol{\mathcal{C}}_1=\dfrac{i\sqrt{\gamma}}{\sqrt{2}\sqrt{\mu}\sqrt{\mathfrak{F}}},\ \boldsymbol{\mathcal{C}}_{-1}=\dfrac{i\sqrt{\gamma}\sqrt{\mathfrak{F}}}{\sqrt{2}\sqrt{\mu}},\ \kappa=-\dfrac{\sqrt{\gamma-4\beta\delta^2\mathfrak{F}}}{2\sqrt{\mathfrak{F}}},\\ \text{Set}^3:\ \boldsymbol{\mathcal{C}}_0=0,\ \boldsymbol{\mathcal{C}}_1=-\dfrac{\sqrt{\gamma}}{2\sqrt{\mu}\sqrt{\mathfrak{F}}},\ \boldsymbol{\mathcal{C}}_{-1}=\dfrac{\sqrt{\gamma}\sqrt{\mathfrak{F}}}{2\sqrt{\mu}},\ \kappa\to\dfrac{\sqrt{-8\beta\delta^2\mathfrak{F}-\gamma}}{2\sqrt{2}\sqrt{\mathfrak{F}}}.\end{cases} \tag{3.21}$$

Type 1: When $\mathfrak{F}<0$, then

$$\boldsymbol{\mathcal{M}}_1(x,t)=\left[\frac{c_1\mathfrak{F}\left(a^2+b^2\mathfrak{F}\right)\operatorname{sech}^2\left(\varpi\sqrt{-\mathfrak{F}}\right)}{\left(a\sqrt{-\mathfrak{F}}\tanh\left(\varpi\sqrt{-\mathfrak{F}}\right)-b\mathfrak{F}\right)\left(a+b\sqrt{-\mathfrak{F}}\tanh\left(\varpi\sqrt{-\mathfrak{F}}\right)\right)}\right], \tag{3.22}$$

$$\boldsymbol{\mathcal{M}}_2(x,t)=\left[\frac{c_1\sqrt{\mathfrak{F}}\left(a^2+b^2\mathfrak{F}\right)\sec^2\left(\varpi\sqrt{\mathfrak{F}}\right)}{\left(a\tan\left(\varpi\sqrt{\mathfrak{F}}\right)-b\sqrt{\mathfrak{F}}\right)\left(a+b\sqrt{\mathfrak{F}}\tan\left(\varpi\sqrt{\mathfrak{F}}\right)\right)}\right]. \tag{3.23}$$

Type 2: When $\mathfrak{F}>0$, then

$$\boldsymbol{\mathcal{M}}_3(x,t)=\left[\frac{c_1\sqrt{\mathfrak{F}}\left(a^2+b^2\mathfrak{F}\right)\sec^2\left(\varpi\sqrt{\mathfrak{F}}\right)}{\left(a\tan\left(\varpi\sqrt{\mathfrak{F}}\right)-b\sqrt{\mathfrak{F}}\right)\left(a+b\sqrt{\mathfrak{F}}\tan\left(\varpi\sqrt{\mathfrak{F}}\right)\right)}\right], \tag{3.24}$$

$$\boldsymbol{\mathcal{M}}_4(x,t)=\left[\frac{c_1\sqrt{\mathfrak{F}}\left(a^2+b^2\mathfrak{F}\right)\csc^2\left(\varpi\sqrt{\mathfrak{F}}\right)}{\left(a\cot\left(\varpi\sqrt{\mathfrak{F}}\right)+b\sqrt{\mathfrak{F}}\right)\left(b\sqrt{\mathfrak{F}}\cot\left(\varpi\sqrt{\mathfrak{F}}\right)-a\right)}\right]. \tag{3.25}$$

Type 3: When $\mathfrak{F}=0$, then

$$\boldsymbol{\mathcal{M}}_5(x,t)=\left[-\frac{c_1\left(\varpi^2\mathfrak{F}+1\right)\left(a^2+b^2\mathfrak{F}\right)}{(a\varpi+b)(b\varpi\mathfrak{F}-a)}\right]. \tag{3.26}$$

Foe above solution sets $\varpi=(\frac{\sqrt{-\boldsymbol{\mathcal{C}}_1^2\mu-2\kappa^2}}{\sqrt{2}\sqrt{\beta}}x+\frac{\kappa(1-\delta)t^{-p}}{\boldsymbol{\mathcal{W}}(\alpha)\sum_{p=0}^{\infty}\left(-\frac{\alpha}{1-\alpha}\right)^p\Gamma(1-\alpha p)})$.

For second set:

Type 1: When $\mathfrak{F}<0$,

$$\boldsymbol{\mathcal{M}}_6(x,t)=\left[\frac{i\sqrt{\gamma}\sqrt{\mathfrak{F}}\left(a^2+b^2\mathfrak{F}\right)\operatorname{sech}^2\left(\varpi\sqrt{-\mathfrak{F}}\right)}{\sqrt{2}\sqrt{\mu}\left(a\sqrt{-\mathfrak{F}}\tanh\left(\varpi\sqrt{-\mathfrak{F}}\right)+b\mathfrak{F}\right)\left(b\sqrt{-\mathfrak{F}}\tanh\left(\varpi\sqrt{-\mathfrak{F}}\right)-a\right)}\right], \tag{3.27}$$

$$\boldsymbol{\mathcal{M}}_7(x,t)=\left[\frac{i\sqrt{\gamma}\sqrt{\mathfrak{F}}\left(a^2+b^2\mathfrak{F}\right)\operatorname{csch}^2\left(\varpi\sqrt{-\mathfrak{F}}\right)}{\sqrt{2}\sqrt{\mu}\left(a\sqrt{-\mathfrak{F}}\coth\left(\varpi\sqrt{-\mathfrak{F}}\right)+b\mathfrak{F}\right)\left(a-b\sqrt{-\mathfrak{F}}\coth\left(\varpi\sqrt{-\mathfrak{F}}\right)\right)}\right]. \tag{3.28}$$

Type 2: When $\mathfrak{F}>0$, then

$$\boldsymbol{\mathcal{M}}_8(x,t)=\left[\frac{i\sqrt{\gamma}\left(a^2+b^2\mathfrak{F}\right)\sec^2\left(\varpi\sqrt{\mathfrak{F}}\right)}{\sqrt{2}\sqrt{\mu}\left(a\tan\left(\varpi\sqrt{\mathfrak{F}}\right)-b\sqrt{\mathfrak{F}}\right)\left(a+b\sqrt{\mathfrak{F}}\tan\left(\varpi\sqrt{\mathfrak{F}}\right)\right)}\right], \tag{3.29}$$

$$\boldsymbol{\mathcal{M}}_9(x,t)=\left[\frac{i\sqrt{\gamma}\left(a^2+b^2\mathfrak{F}\right)\csc^2\left(\varpi\sqrt{\mathfrak{F}}\right)}{\sqrt{2}\sqrt{\mu}\left(a\cot\left(\varpi\sqrt{\mathfrak{F}}\right)-b\sqrt{\mathfrak{F}}\right)\left(a+b\sqrt{\mathfrak{F}}\cot\left(\varpi\sqrt{\mathfrak{F}}\right)\right)}\right]. \tag{3.30}$$

Type 3: When $\mathfrak{F}=0$, then

$$\boldsymbol{\mathcal{M}}_{10}(x,t)=\left[-\frac{i\sqrt{\gamma}\left(\varpi^2\mathfrak{F}+1\right)\left(a^2+b^2\mathfrak{F}\right)}{\sqrt{2}\sqrt{\mu}\sqrt{\mathfrak{F}}(a\varpi+b)(b\varpi\mathfrak{F}-a)}\right]. \tag{3.31}$$

Foe above set $\varpi=\delta x+\frac{-\frac{\sqrt{\gamma-4\beta\delta^2\mathfrak{F}}}{2\sqrt{\mathfrak{F}}}(1-\delta)t^{-p}}{\boldsymbol{\mathcal{W}}(\alpha)\sum_{p=0}^{\infty}\left(-\frac{\alpha}{1-\alpha}\right)^p\Gamma(1-\alpha p)}$.

4. Qualitative analysis

4.1. Bifurcation analysis

In this section, we have examined the two-dimensional dynamical system in the phase-plane by conceptualizing the bifurcation theory [32]. By incorporating the Galilean transformation, we determine a planar dynamical system, which can be described as

$$\begin{cases}\dfrac{d\boldsymbol{\mathcal{N}}}{d\varpi}=\boldsymbol{\mathcal{S}},\\ \dfrac{d\boldsymbol{\mathcal{S}}}{d\varpi}=-\Upsilon_1\boldsymbol{\mathcal{N}}^3+\Upsilon_2\boldsymbol{\mathcal{N}},\ \Upsilon_1=\dfrac{\gamma}{(\kappa^2+\beta\delta^2)},\ \Upsilon_2=\dfrac{\mu}{(\kappa^2+\beta\delta^2)}.\end{cases} \tag{4.1}$$

The equilibria points for the system (4.1) are:

$$\mathfrak{B}_1(\boldsymbol{\mathcal{N}},\boldsymbol{\mathcal{S}})=\mathfrak{B}_1(0,0),\ \mathfrak{B}_2(\boldsymbol{\mathcal{N}},\boldsymbol{\mathcal{S}})=\mathfrak{B}_2\left(-\frac{i\sqrt{\Upsilon_2}}{\sqrt{\Upsilon_2}},0\right),\ \mathfrak{B}_3(\boldsymbol{\mathcal{N}},\boldsymbol{\mathcal{S}})=\mathfrak{B}_3\left(\frac{i\sqrt{\Upsilon_2}}{\sqrt{\Upsilon_1}},0\right). \tag{4.2}$$

The Jacobian of the system (4.2) is of the form:

$$\boldsymbol{\mathcal{J}}(\boldsymbol{\mathcal{N}},\boldsymbol{\mathcal{S}}) = \begin{vmatrix} 0 & 1 \\ -3\Upsilon_1^2\boldsymbol{\mathcal{N}}^2 - \Upsilon_2 & 0 \end{vmatrix} = 3\Upsilon_1^2\boldsymbol{\mathcal{N}}^2 + \Upsilon_2. \tag{4.3}$$

The determinant and trace of (4.3) at the equilibria points $\mathfrak{B}_i(\boldsymbol{\mathcal{N}},\boldsymbol{\mathcal{S}})$ are indicated by $\boldsymbol{\mathcal{D}}$ and $\boldsymbol{\mathcal{T}}$, respectively, and these are presented as follows:

$$\begin{aligned} \boldsymbol{\mathcal{T}} &= \operatorname{trace}(\boldsymbol{\mathcal{T}})_{\mathfrak{B}_i} = 0, \\ \boldsymbol{\mathcal{D}} &= \det(\boldsymbol{\mathcal{T}})_{\mathfrak{B}_i} = 3\Upsilon_1^2\boldsymbol{\mathcal{N}}^2 + \Upsilon_2. \end{aligned}$$

The critical point is categorized as a saddle when $\boldsymbol{\mathcal{D}} < 0$, a central point when $\boldsymbol{\mathcal{D}} > 0$ and $\boldsymbol{\mathcal{T}} = 0$, a cusp when $\boldsymbol{\mathcal{D}} = 0$, and a node if $\boldsymbol{\mathcal{D}} > 0$ and $\boldsymbol{\mathcal{T}}_2 - 4\boldsymbol{\mathcal{D}} > 0$.

Let us examine various parameter configurations for system (4.1) in order to study the dynamical system's phase plane. The Table 1 signify the distinct behavior of phase dynamics of proposed system (4.1).

Table 1. Behavior of equilibrium points (EPs) under distinct parameter conditions.

Case	**Parameter conditions**	**Equilibrium points**	**Nature of EPs**	**Figure Ref.**
(i)	$\Upsilon_1 < 0,\ \Upsilon_2 > 0$	$(0,0)$, $(1,0)$, $(-1,0)$	$(0,0)$ is a saddle; $(1,0)$ and $(-1,0)$ behave as centers	Figure 2(a)
(ii)	$\Upsilon_1 > 0,\ \Upsilon_2 < 0$	$(0,0)$, $(-1,0)$, $(1,0)$	$(0,0)$ is a center; $(-1,0)$ and $(1,0)$ are saddles	Figure 2(b)
(iii)	$\Upsilon_1 < 0,\ \Upsilon_2 < 0$	$(0,0)$	Single EP at $(0,0)$, acting as a center,	Figure 2(c)
(iv)	$\Upsilon_1 > 0,\ \Upsilon_2 < 0$	$(0,0)$	Single EP at $(0,0)$, indicating saddle-like nature, providing periodic motion in its vicinity	Figure 2(d)

Equilibrium points (EPs) are critical in comprehending the qualitative structure of dynamical systems. They show the states at which the system remains constant over time. The local behavior near an EP represents the stability and nature of the system in its vicinity. A saddle point is an unstable equilibrium point where trajectories approach the point along specific directions and diverge along others, showing overall instability. A center is a neutrally stable point surrounded by closed orbits, meaning that trajectories neither converge to nor diverge from the EP, but instead show sustained oscillatory structure. Although not provide in the present analysis, other common kinds of equilibrium points include nodes and spirals (foci). Nodes, whose paths converge to or diverge from the EP without oscillation, can be either stable or unstable. Spiral points indicate damped or amplified oscillations by displaying a spiral motion of trajectories either toward (stable focus) or away from (unstable focus) the equilibrium. Determining the system's sensitivity to starting conditions and long-term behavior requires an understanding of EPs.

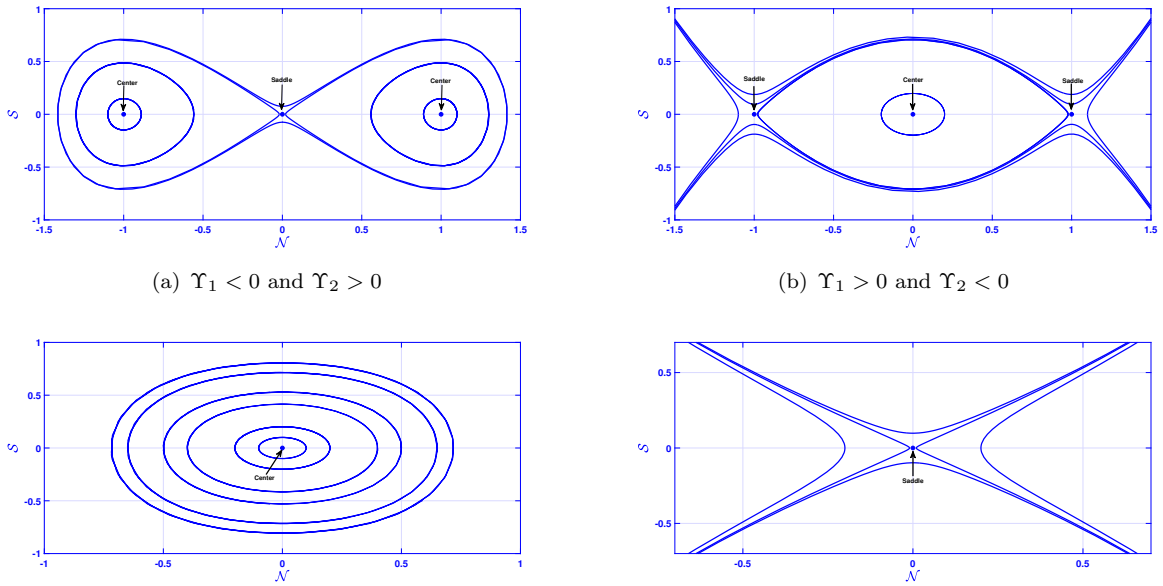

(a) $\Upsilon_1 < 0$ and $\Upsilon_2 > 0$ (b) $\Upsilon_1 > 0$ and $\Upsilon_2 < 0$

(c) $\Upsilon_1 < 0$ and $\Upsilon_2 < 0$ (d) $\Upsilon_1 > 0$ and $\Upsilon_2 > 0$

Figure 2. Phase portraits corresponding to distinct cases of parameter values representing the nature of EPs.

4.2. Chaos and some other novel characteristics

This section will analyze the chaotic structures of the modified system defined below:

$$\begin{cases} \dfrac{d\boldsymbol{\mathcal{N}}}{d\varpi} = \boldsymbol{\mathcal{S}}, \\ \dfrac{d\boldsymbol{\mathcal{S}}}{d\varpi} = -\Upsilon_1 \boldsymbol{\mathcal{N}}^3 + \Upsilon_2 \boldsymbol{\mathcal{N}} + \boldsymbol{\mathcal{Y}} \sin(\boldsymbol{\mathcal{W}}), \\ \dfrac{d\boldsymbol{\mathcal{W}}}{d\varpi} = \boldsymbol{\mathcal{Z}}\varpi. \end{cases} \tag{4.4}$$

In this study, $\boldsymbol{\mathcal{Y}}$ represents the frequency of vibration, while $\boldsymbol{\mathcal{Z}}$ shows the degree of the external disturbances. In the Figures 2-5, we represent the dynamics of the system (4.4) with varying $\boldsymbol{\mathcal{Y}}$ and $\boldsymbol{\mathcal{Z}}$, where other parameters are fixed as: $\gamma = -4.73$, $\mu = -.4$, $\kappa = 4.19$, $\beta = -3.9$, $\delta = 3.9$. Figure 3 demonstrates the physical dynamics of the system by providing a combination of 2D and 3D phase portraits, time series, and a Poincaré section, determined by varying the parameters Υ_1 and Υ_2. The 2D phase portrait depicted in subplot (3(a)) reflects a nested loop nature in the $(\mathcal{N}, \mathcal{S})$ plane, which is represented of quasi-periodic motion. The trajectories do not close on themselves but remain confined within a bounded region, revealing the influence of two or more incommensurate frequencies. Subplot (3(b)) demonstrates the 3D phase space projection over time, reinforcing the quasi-periodic structure through a structured, toroidal trajectory that does not show the randomness features of chaos. The time series demonstrated in subplot (3(c)) displays a modulated oscillatory pattern, where the signal depicts regularity but lacks exact repetition, again pointing to quasi-periodic structure. Subplot (3(d)) represents the Poincaré section in the $(\mathcal{N}, \mathcal{S})$ plane, where the formation of a closed ring of scattered points suggests strong evidence of quasi-periodicity. Unlike chaotic attractors, which produce scattered and irregular point clouds, or periodic systems, which yield a finite set of discrete points, the determined ring

behavior confirms the existence of sustained, non-repeating oscillations. Figure 4 displays the

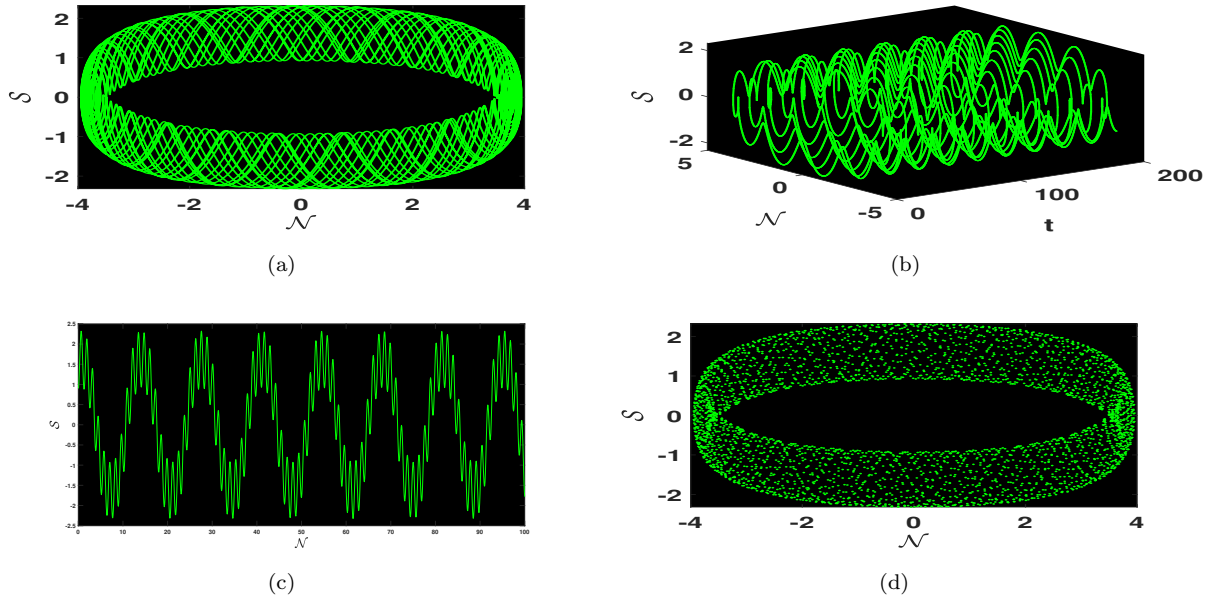

Figure 3. Physical dynamics of chaos are illustrated using 2D and 3D, time series and poincare phase portraits for system (4.4) obtained by varying the values of $\Upsilon_1,\ \Upsilon_2$.

physical dynamics of the system (4.4). Subplot (4(a)) represents the 2D phase portrait in the $(\mathcal{N}, \mathcal{S})$ plane, where the trajectory forms a torus-like nested loop behavior. The loops are densely packed and do not repeat exactly, which shows a quasi-periodic pattern. This is suggested by subplot (4(b)), the 3D trajectory in $(t, \mathcal{N}, \mathcal{S})$ space, which forms a structured and smooth surface without the randomness typically seen in chaotic motion. Subplot (4(c)) represents the time series of $\mathcal{S}$ versus $\mathcal{N}$, showing a modulated waveform that lacks strict periodicity but retains a discernible pattern, further reinforcing the quasi-periodic pattern. Lastly, the Poincaré section in subplot (4(d)) shows a well-defined, structured distribution of points along a ring with complex internal patterns. This structured appearance, without erratic scattering, verifies that the system resides in a quasi-periodic pattern. The consistency across all subplots provides the system shows stable quasi-periodic motion under the provided parameter values, with no indications of either periodic locking or chaotic divergence. Figure 5 suggests the physical dynamics of the system under the influence of varying parameters Υ_1 and Υ_2. In subplot (10(a)), the 2D phase portrait in the $(\mathcal{N}, \mathcal{S})$ plane forms a densely packed toroidal behavior, representing quasi-periodic oscillations with multiple incommensurate frequencies. The trajectory does not close onto itself, and the nested loops appear neither periodic nor random, verifying the presence of quasi-periodic motion. The 3D plot in subplot (11(a)) further illustrates this interpretation, as the trajectory in $(t, \mathcal{N}, \mathcal{S})$ space winds around smoothly in a structured tube-like fashion, properties of quasi-periodic orbits. The time series represented in subplot (5(c)) reveals a modulated waveform with an amplitude envelope that varies in a smooth but non-repeating pattern, reinforcing the quasi-periodic pattern. Finally, the Poincaré section in subplot (5(d)) depicts a series of discrete, non-overlapping points distributed in a ringed, torus-like formation, different from the scattered points typically related with chaos and the fixed clusters of periodic motion. Figure 6 represents a series of 2D phase portraits for system (2.14), demonstrating the system's

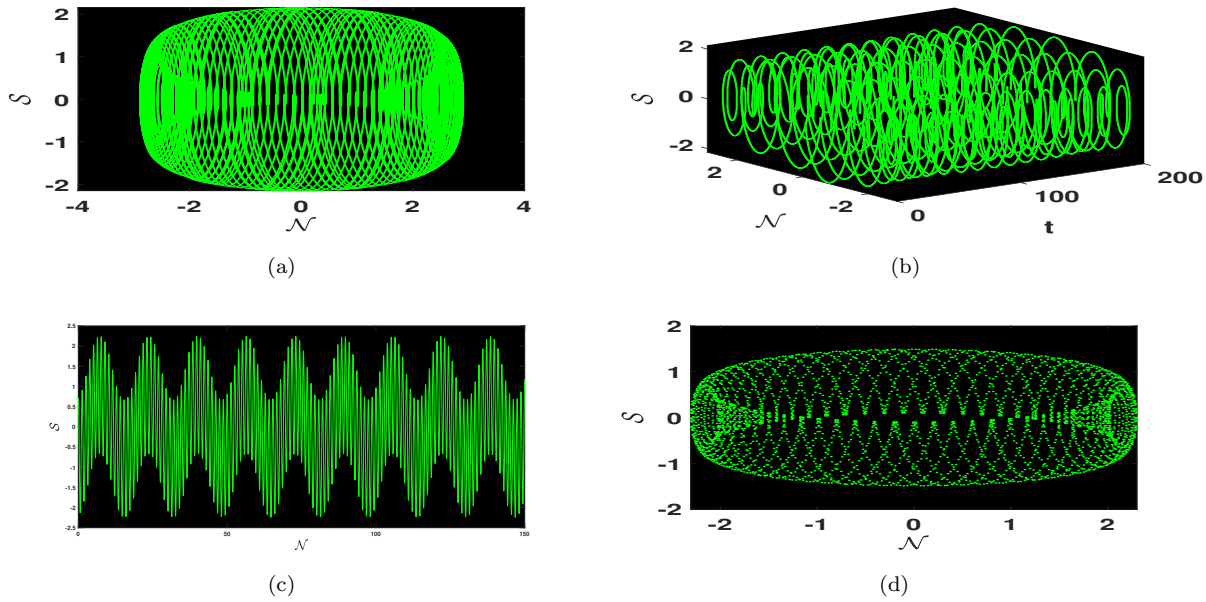

Figure 4. Physical dynamics of chaos are illustrated using 2D and 3D, time series and poincare phase portraits for system (4.4) obtained by varying the values of $\Upsilon_1,\ \Upsilon_2$.

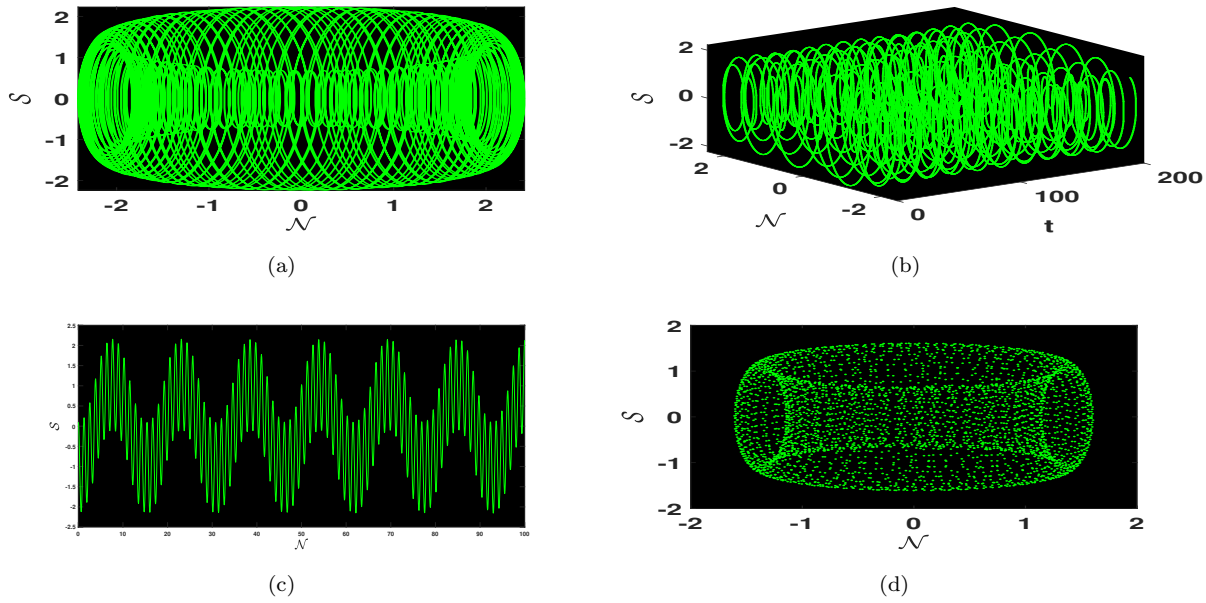

Figure 5. Physical dynamics of chaos are illustrated using 2D and 3D, time series and poincare phase portraits for system (4.4) obtained by varying the values of $\Upsilon_1,\ \Upsilon_2$.

dynamic nature under varying values of Υ_1 and Υ_2. Subfigures 6(e), 6(f), and 7(a) demonstrate complex, non-repeating trajectories that are indicative of chaotic dynamics, where the system depicts sensitivity to distinct initial conditions and irregular oscillations. In contrast, subfigures 7(b) and 8(a) signify quasi-periodic structure, characterized by structured yet non-repeating

closed loops, revealing an intermediate state between order and chaos. Subfigure 8(b) reflects a more periodic-like, where the phase space trajectory becomes more symmetric, providing a transition from chaos to a more ordered dynamical regime. These patterns collectively reveal the rich and diverse pattern of the system as influenced by changes in the control parameters. Figures 7 and 8 demonstrate the complex nature of the system elaborated by Eq. (4.1) through

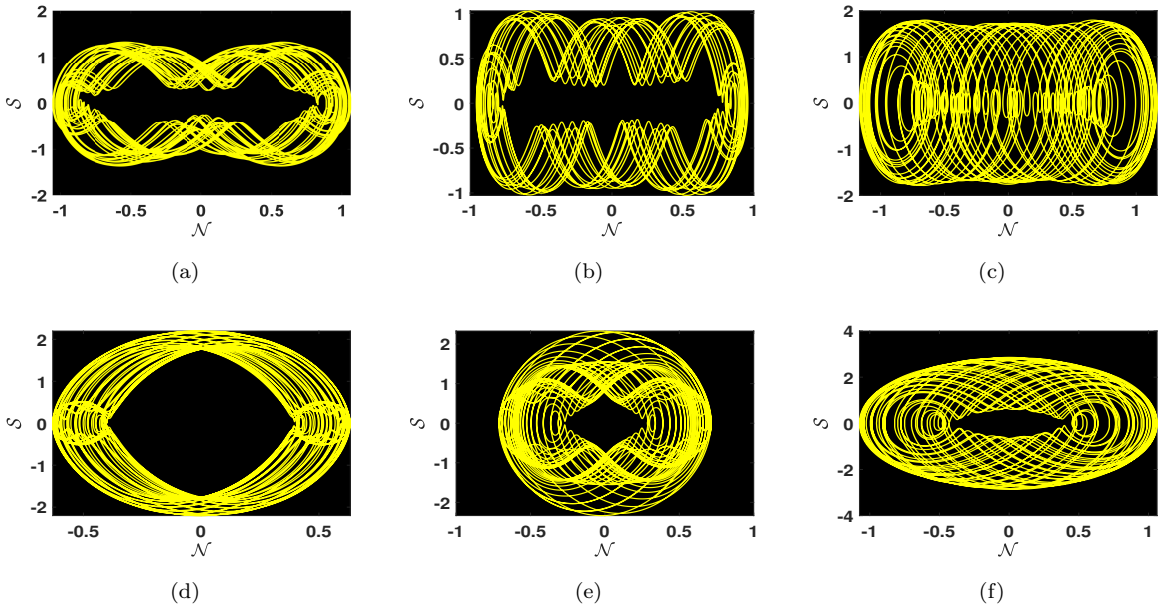

Figure 6. Physical dynamics of chaos are shown using 2D phase portraits for system (4.4) obtained by varying the values of $\Upsilon_1,\ \Upsilon_2$.

return map and strange attractor analysis, respectively. In Figure 7, the return map graphs for distinct time delays τ reflect transitions in the system's temporal correlations. For $\tau = 2$ (Figure 7(a)), the system demonstrates a near-linear and correlated pattern, indicating low-dimensional quasi-periodic dynamics. However, for $\tau = 50$ (Figure 7(b)), the nature becomes more dispersed and irregular, showing the emergence of intricate and potentially chaotic structure due to increased temporal separation. Figure 8 demonstrates the phase space evolution

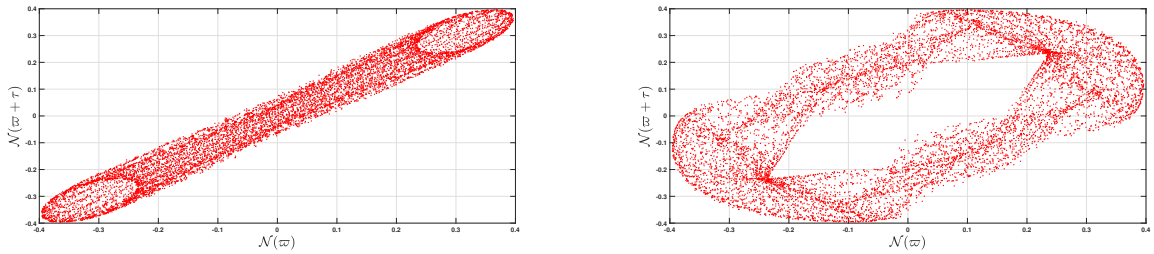

(a) $\tau = 2$ with initial condition (0.08, -0.62, 0.36)

(b) $\tau = 50$ with initial condition (0.08, -0.62, 0.36)

Figure 7. Physical dynamics of return map analysis of the system described by Eq. (4.1) achieved with the values of parameters as $\gamma = -7.73,\ \mu = -2.4,\ \kappa = 4.19,\ \beta = -3.9,\ \delta = 3.9,\ \Upsilon_1 = 7.91,\ \Upsilon_2 = 9.9$.

in 3D, representing the formation of strange attractors under distinct initial conditions. Both

subfigures 8(a) and 8(b) depict densely folded and stretched trajectories, which are characteristic of chaotic attractors. The sensitivity to initial conditions is evident as slight changes lead to significantly distinct geometric structures in the attractor. These graphs demonstrate that, within the specified parameter domain, the system demonstrates rich nonlinear dynamics with compelling evidence of chaos and unpredictability. In Figure 9, we study the chaotic nature

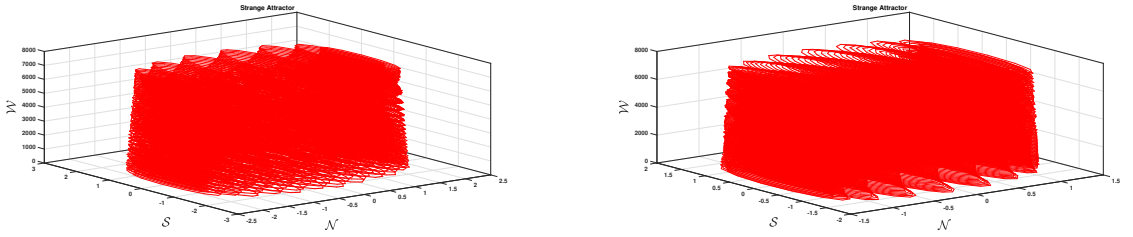

(a) with initial condition (0.48, 0.03, -0.4) (b) with initial condition (0.48, -0.3, -1.4)

Figure 8. Physical dynamics of strange attractor analysis of the system described by Eq. (4.1) achieved with the values of parameters as $\gamma = -7.73,\ \mu = -2.4,\ \kappa = 4.19,\ \beta = -3.9,\ \delta = 3.9,\ \Upsilon_1 = 7.91,\ \Upsilon_2 = 9.9$.

of the system presented by Eq. (4.1) using multiple diagnostic tools. These tools help assess the underlying nonlinear dynamics and verify the existence of chaos from distinct perspectives. Subfigure 9(a) provides the evolution of Lyapunov exponents over time. The convergence of one exponent approaches a positive value, while others remain near negative or zero, is a strong indicator of chaotic dynamics and sensitivity to initial conditions. Subfigure 9(b) represents the box-counting method used to compute the fractal dimension. The nonlinear scaling analyzed in the plot reflects the complexity of the attractor and confirms its fractal behavior, which is a key signature of chaos. Subfigure 9(c) displays the recurrence plot, revealing regularly and intricate spaced patterns that present qualitative evidence of deterministic yet non-periodic structure in the system. Finally, the power spectrum analysis is displayed in subfigure 9(d), where a wide frequency distribution devoid of prominent peaks validates the existence of broadband chaotic signals and aperiodicity.

4.3. Sensitivity analysis

In this section, we focus on assessing the sensitivity analysis of the presenting system (4.4) in the context of a numerical method, namely, the Runge–Kutta method [14]. Sensitivity analysis is essential to comprehending how changes in initial conditions and parameter values affect nonlinear systems' overall dynamics. It is useful to determine which initial states or characteristics have a major impact on the stability of the system or cause divergent behaviors like chaos, quasi-periodicity, or stable periodic oscillations. Reviewing and contrasting the multiple solution curves for distinct initial conditions, while keeping the parameter values fixed at $\gamma = 0.2$, $\kappa = 0.3$, $\beta = -0.001$, $\delta = 0.3$, and $\mu = 0.3$, shows notable differences in the system's evolution, as depicted in Figures 10-11.

In Figure 10, two trajectories are generated from different initial conditions: (0.5, 0, 0) (orange) and (0, 0.7, 0) (yellow). Despite identical parameters, the system demonstrates substantially distinct behavior in its temporal evolution, elaborating its sensitivity to initial configurations. Figure 11 further provides this observation by presenting three solution trajectories arising from distinct initial conditions: (2.35, 0, 0) (yellow), (0, 1.58, 0) (orange), and (5.1, 0.1, 0)

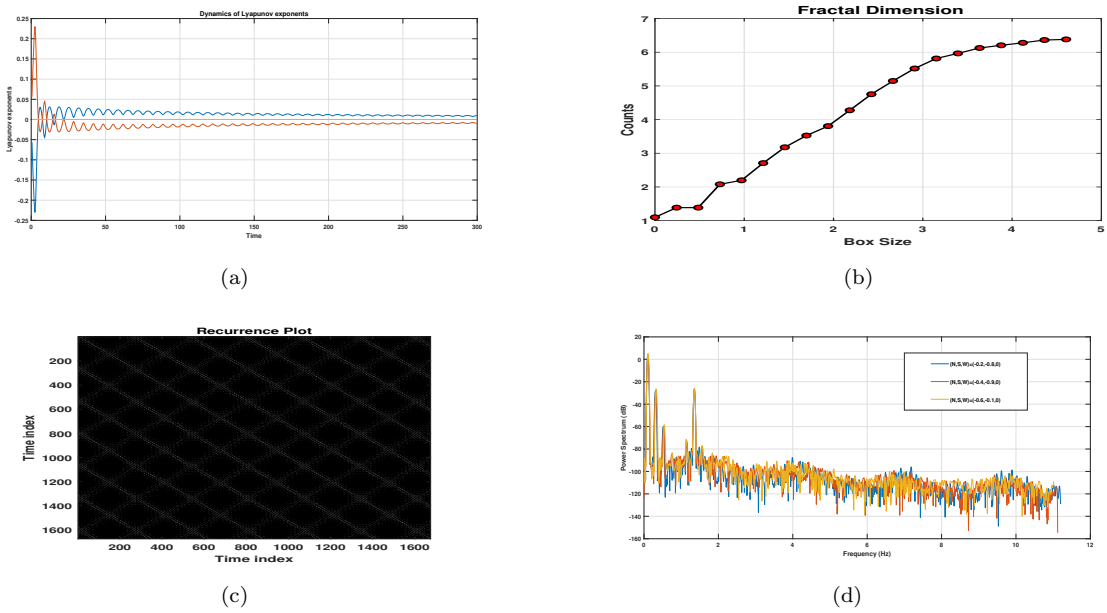

(a) (b) (c) (d)

Figure 9. Physical dynamics of various dynamical characteristics of the system described by Eq. (4.1) achieved with the values of parameters as $\gamma = -7.73,\ \mu = -2.4,\ \kappa = 4.19,\ \beta = -3.9,\ \delta = 3.9,\ \Upsilon_1 = 2.91,\ \Upsilon_2 = 7.21.$

(black). These trajectories' divergence over time highlights the system's great sensitivity and the possibility of complicated dynamics, even with minor initial state perturbations. This sensitivity analysis serves as a prelude to additional research utilizing bifurcation and chaos theory and demonstrates how responsive the nonlinear system is to initial inputs.

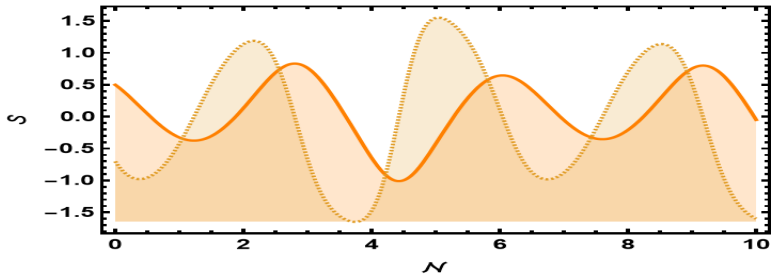

(a)

Figure 10. The system described by Eq. (4.1) was subjected to a sensitivity analysis by choosing two different initial conditions: (0.5, 0, 0) (orange), and (0, 0.7, 0) (yellow).

5. Physical interpretation of solutions

In this section, we present a comprehensive physical interpretation of the analytical soliton solutions obtained for the FGRDM using Atangana's conformable derivative. To better analyze and visualize the spatial nature of these solutions, we have provided 2D, 3D, and contour plots in Figures 12–18. These visual representations not only verify the mathematical correctness of the solutions but also shed light on their physical relevance in demonstrating real-world wave phenomena in nonlinear and dissipative media. Figure 12 represents a dark soliton solution, featured by a localized dip in amplitude within an otherwise constant background. This type of solution

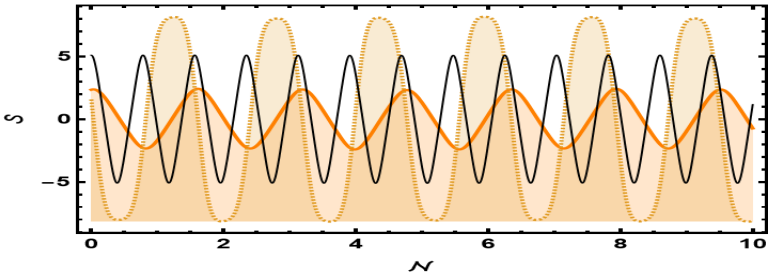

(a)

Figure 11. The system described by Eq. (4.4) was subjected to a sensitivity analysis by choosing three different initial conditions: (2.35, 0, 0) (yellow), (0, 1.58, 0) (orange), and (5.1, 0.1, 0) (black).

is commonly determined in Bose–Einstein condensates and optical fibers, where the wave amplitude momentarily reduces due to phase shifts or dispersion effects. The physical implication of such solutions lies in their stability and robustness under specific initial or boundary conditions. Figure 13 represents an M-shaped solution, indicating a multi-peak wave profile with symmetry. This form can be interpreted as a localized wave packet with internal oscillations, potentially simulating energy localization in nonlinear lattices or layered mechanical behaviors. The sharp crests provide strong nonlinear interactions or resonances in the system. Figure 14 represents a periodic wave solution, which elaborate sustained, repeating oscillatory structure over space or time. These solutions are related in systems where energy is periodically transferred, including climate oscillations, electrical circuits, or vibrating beams. The periodic nature suggests the possibility of recurring, stable dynamics within the nonlinear fractional-order system. In Figure 15, we analyze a hyperbolic-type solution, which typically arises in scenarios including wavefront propagation or kink-type behaviors. These solutions often model shock waves, domain walls, or transition fronts in biological and physical systems. The hyperbolic form shows sharp transitions between two stable states of the system. Figure 16 represents a combo-type solution, where multiple wave structures coexist. This hybrid profile represents complex interactions between dispersive, nonlinear, and memory effects intended by the fractional derivative. Such propogation may occur in fluid mechanics or nonlinear optics when wave modes interact. Figure 17 again indicates a periodic solution, reinforcing the diversity of periodic natures permissible under distinct parameter regimes. Its presence demonstrates the parameter sensitivity of the model and provides opportunities for controlled oscillatory structures in applied systems. Lastly, Figure 18 represents a mixed trigonometric solution, combining cosine and sine forms. These behaviors can represent spatially oscillating fields or interference patterns, associate in quantum mechanics, acoustics, and electromagnetics. The mixed trigonometric form provides constructive and destructive interference in nonlinear wave environments. The visualization of these solutions in both 2D and 3D, along with contour plots, allows a deeper comprehending of their localized structure, symmetry, periodicity, and amplitude modulation. Each solution not only enriches the analytical spectrum of the FGRDM but also presents meaningful insights into its potential applications across engineering, physics, and applied mathematics.

5.1. Comparison with existing literature

The current study introduces a novel analysis of the FGRDM using Atangana's conformable derivative, addressing both analytical and qualitative aspects. Unlike previous studies that

largely emphasize only certain type of traveling wave solutions, our approach not only generates a broader class of exact soliton solutions through a hybrid analytical framework (Riccati sub-equation technique combined with the Riccati–Bernoulli sub-ODE technique) but also offers a deep investigation into the chaotic structure of the system. We incorporate an extended set of chaos detection tools such as Poincaré sections, recurrence plots, time series, power spectra, return maps, strange attractors and fractal dimension, thereby providing a comprehensive dynamic profile of both perturbed and unperturbed versions of the model. A detailed comparison between the current work and the recent article [27] is presented in Table 2. This comparison indicates the advancements and broader scope of our present research.

Table 2. Comparison of our work with existing literature.

Feature	Said et al. [27]	**Current work**
Fractional operator used	Conformable fractional derivative	Atangana's Conformable Derivative
Analytical techniques	Extended $(\frac{G'}{G})$-expansion method	Riccati sub-equation + Riccati–Bernoulli sub-ODE method (hybrid approach)
Derived solutions	Limited to optical traveling wave forms	Wide variety of soliton solutions such as periodic, hyperbolic, M-shape, dark, combo, and trigonometric types
Qualitative analysis	Not included	Comprehensive bifurcation and chaos analysis
Chaos detection tools	Not discussed	Time series, Poincaré map, power spectrum, return map, strange attractor, recurrence plot, fractal dimension
Graphical representations	2D plots only	2D, 3D, and contour plots for physical interpretation
Significance	Focus on optical transmission stability	Broad applicability to soliton theory, nonlinear dynamics, and chaotic system behavior

6. Conclusion

In conclusion, we have successfully studied the fractional generalized reaction Duffing model (FGRDM) with Atangana's conformable derivative, which provides a useful framework for simulating systems with memory and hereditary effects. We employed two effective analytical techniques, namely, the Riccati sub-equation method and the Riccati–Bernoulli sub-ODE method, to construct a wide variety of exact soliton solutions. These solutions reveal the rich nonlinear behavior of the model and represent its potential for revealing complex wave phenomena. Moreover, we analyzed a detailed qualitative analysis of both the perturbed and unperturbed forms of the model. Through bifurcation and chaos analysis, we illustrated how small changes in system parameters or initial conditions can lead to important changes in system behavior. To further study the chaotic dynamics, we used different diagnostic tools, involving time series plots, Poincaré sections, power spectra, return maps, strange attractors, recurrence plots,

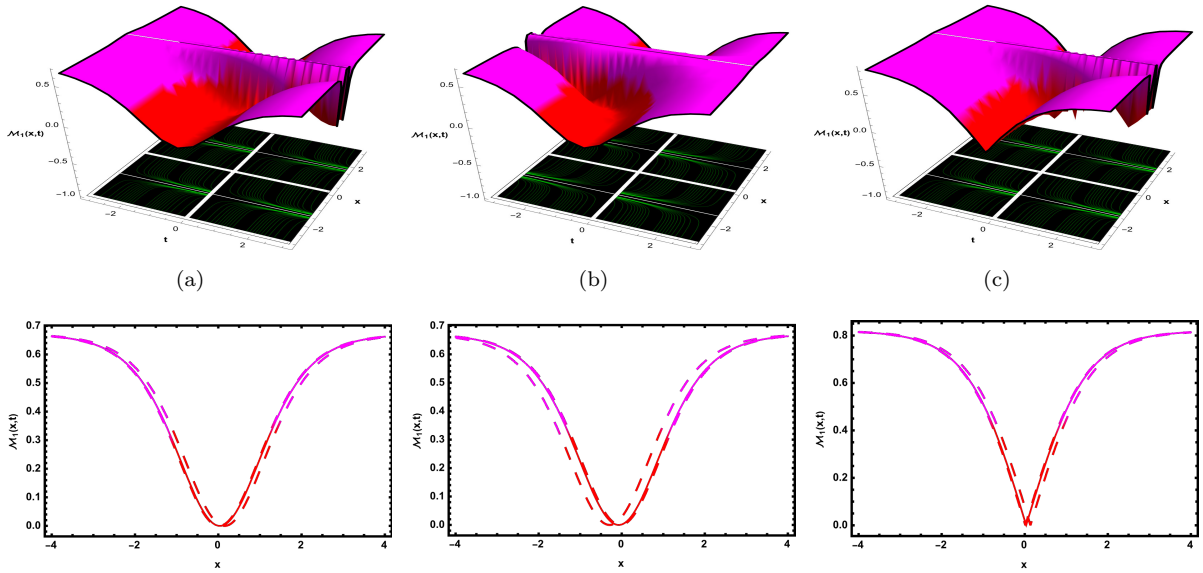

(a) (b) (c)

(d) $\alpha = 0.5$ (e) $\alpha = 0.6$ (f) $\alpha = 0.7$

Figure 12. Physical depiction of dark type solution (3.5) under certain parameter $\sigma = -0.5$, $\beta = 0.9$, $\kappa = 0.7$, $\mu = 0.8$, $\delta = 0.23$.

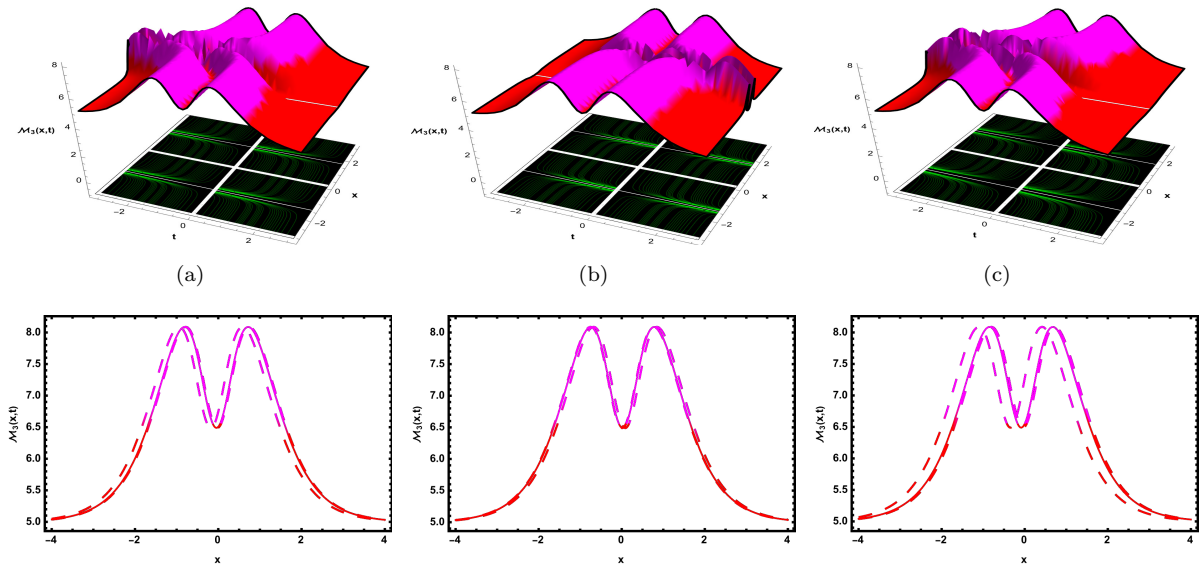

(a) (b) (c)

(d) $\alpha = 0.2$ (e) $\alpha = 0.4$ (f) $\alpha = 0.6$

Figure 13. Physical depiction of $M-$shape solution (3.7) under certain parameter $\sigma = -1.3$, $\beta = 0.6$, $\kappa = 0.3$, $\mu = 0.2$, $\delta = 0.7$.

and fractal dimension analysis. These tools collectively presented strong evidence of chaos and helped uncover the underlying nature of the model's dynamics. The results provide valuable insight for researchers working in applied mathematics, engineering, and physics, particularly those interested in complex wave structure and chaotic systems. Despite the effectiveness of the presented hybrid analytical approach, some limitations should be acknowledged. The Riccati

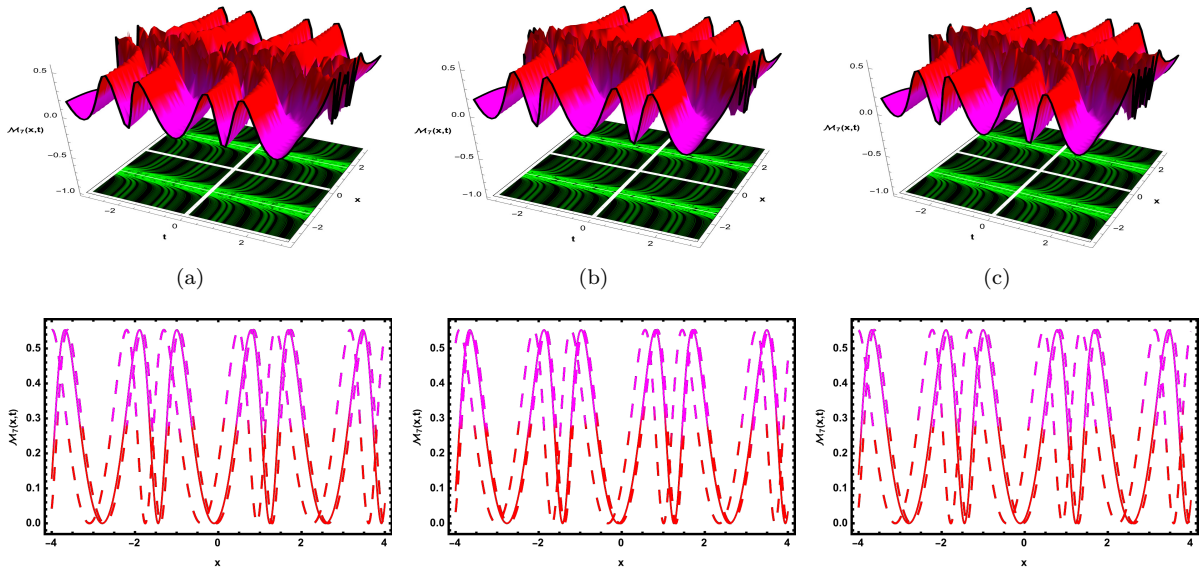

(a) (b) (c)

(d) $\alpha = 0.2$ (e) $\alpha = 0.3$ (f) $\alpha = 0.9$

Figure 14. Physical depiction of periodic solution (3.11) under certain parameter $\sigma = 2.8,\ \delta = 0.7,\ \kappa = 0.3,\ Q = 0.2,\ R = 0.4,\ \mu = 0.2$.

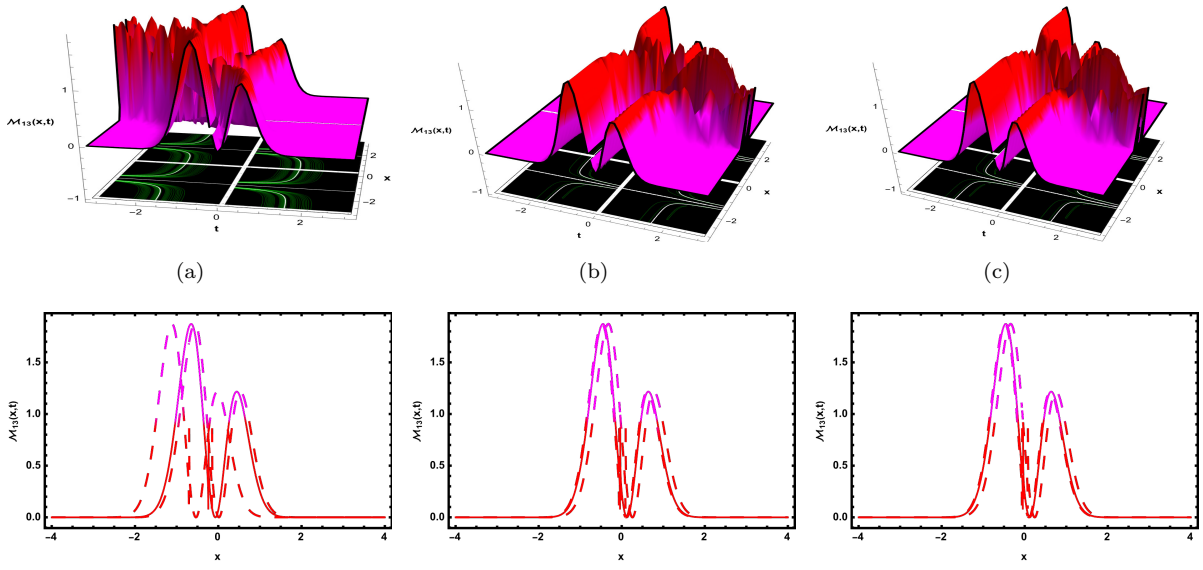

(a) (b) (c)

(d) $\alpha = 0.5$ (e) $\alpha = 0.6$ (f) $\alpha = 0.7$

Figure 15. Physical depiction of hyperbolic type solution (3.17) under certain parameter $\sigma = 1.8,\ \delta = 0.3,\ \kappa = 0.8,\ \mu = 0.32,\ R = 0.2,\ Q = 0.9$.

and Riccati–Bernoulli sub-ODE methods rely on specific transformation assumptions and may not describe all possible solution forms under complex or perturbed conditions. Furthermore, the Atangana conformable derivative, while advantageous for modeling memory effects, can be sensitive to parameter choices and lacks extensive experimental validation. In the future, this research can be expanded by considering the FGRDM in higher-dimensional settings or coupled

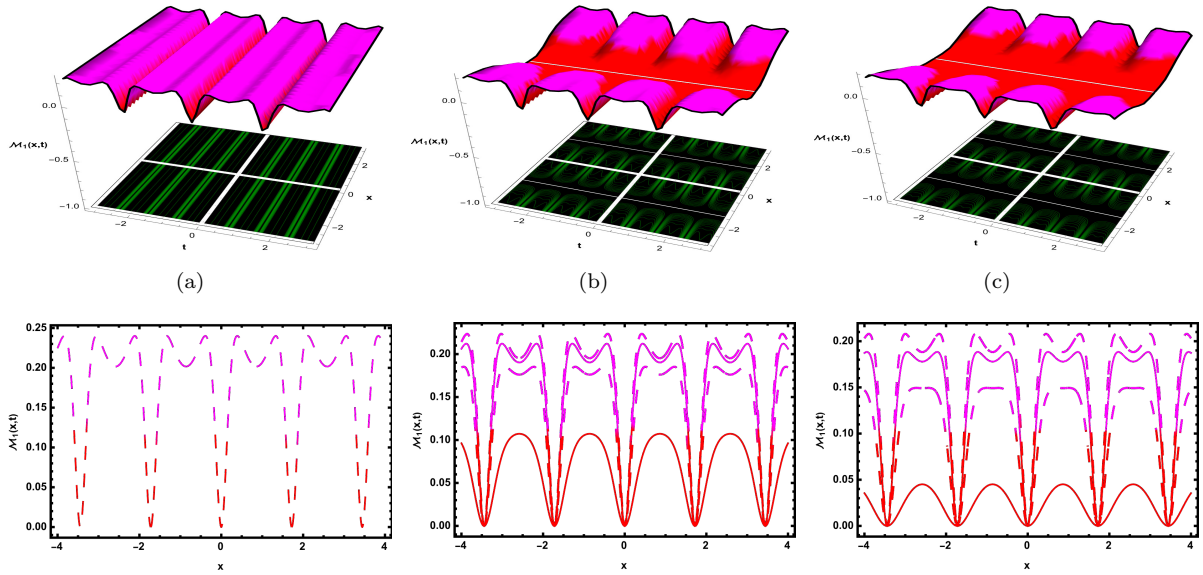

(a) (b) (c)

(d) $\alpha = 0.5$ (e) $\alpha = 0.4$ (f) $\alpha = 0.26$

Figure 16. Physical depiction of combo type solution (3.22) under certain parameter $\mathfrak{F} = -0.8,\ a = 0.9,\ b = 0.3,\ \kappa = 0.62,\ \mu = 0.7,\ c_1 = 0.3.$

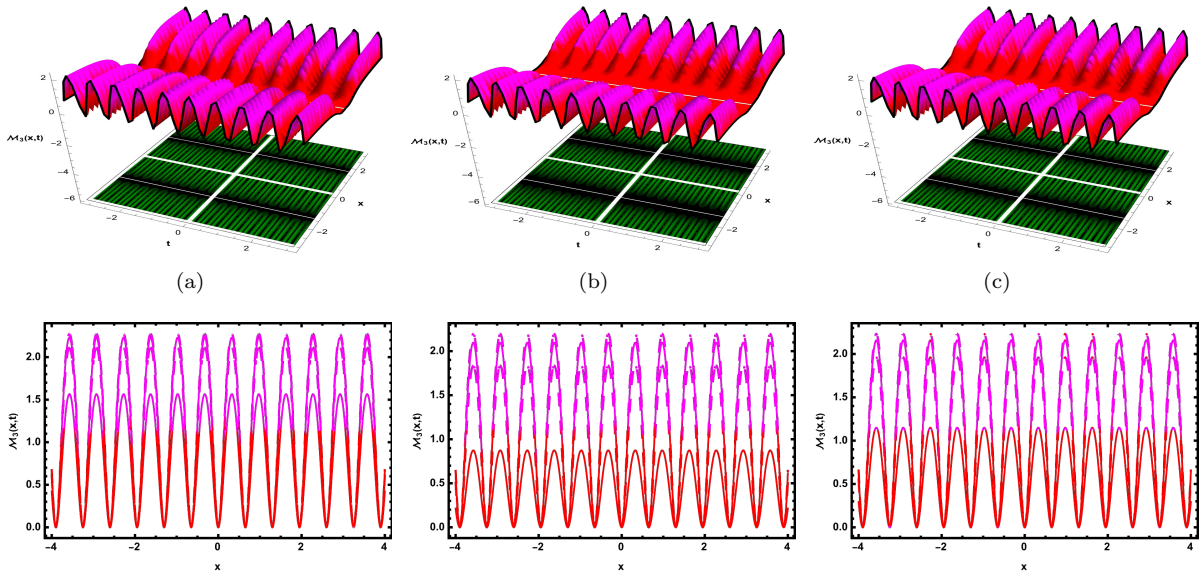

(a) (b) (c)

(d) $\alpha = 0.53$ (e) $\alpha = 0.63$ (f) $\alpha = 0.73$

Figure 17. Physical depiction of periodic solution (3.24) under certain parameter $\mathfrak{F} = 3.4,\ a = 0.8,\ b = 0.7,\ \kappa = 0.62,\ \mu = 0.7,\ c_1 = -0.93,\ \beta = 0.4.$

systems. Furthermore, investigating the model under different types of fractional derivatives (such as Caputo or Caputo–Fabrizio) may provide further insights. Finally, the incorporation of stochastic effects or time-delay terms could present a more realistic representation of physical systems and lead to deeper comprehension of real-world chaotic dynamics.

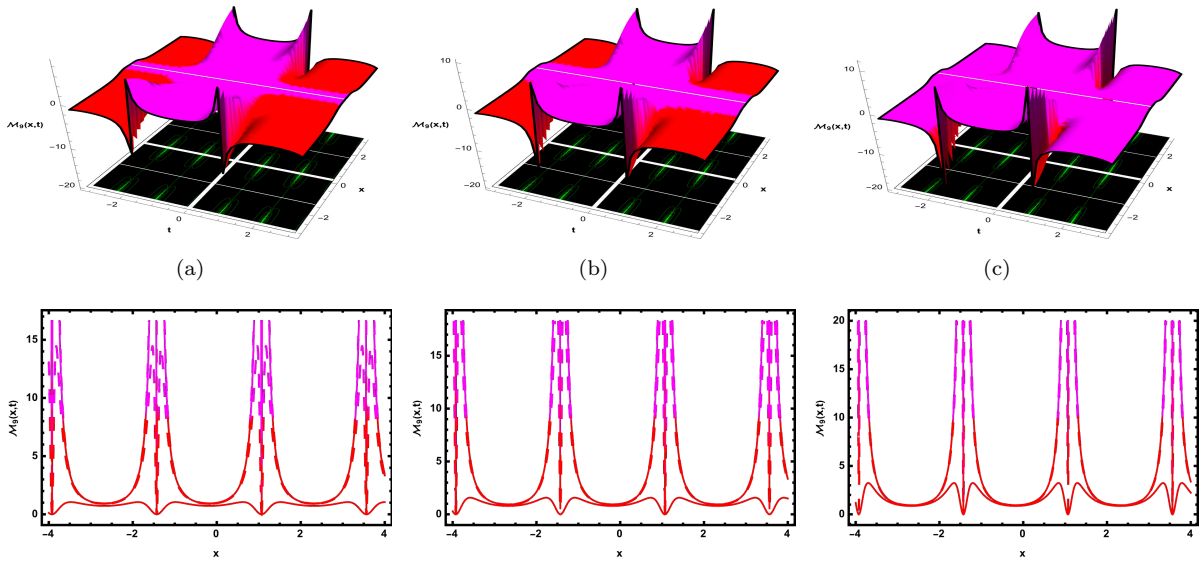

(a) (b) (c)

(d) $\alpha = 0.3$ (e) $\alpha = 0.35$ (f) $\alpha = 0.4$

Figure 18. Physical depiction of mixed trigonometric solution (3.30) under certain parameter $\mathfrak{F} = 4.4,\ a = 0.5,\ b = 0.3,\ \gamma = 0.2,\ \mu = 0.43,\ \delta = 0.3,\ \beta = 0.4$.

Declarations

Conflict of interest. The authors declare that they have no conflict of interest.

Data availability. No data was used or generated in the paper.

Acknowledgment. The authors thank Deanship of Scientific Research at Imam Mohammad Ibn Saud Islamic University (IMSIU).

Funding. This work was supported and funded by the Deanship of Scientific Research at Imam Mohammad Ibn Saud Islamic University (IMSIU) (grant number IMSIU-DDRSP2604).

References

[1] S. Akram, S. Taoufik and M. ur Rahman, *Unraveling symmetry, bifurcation dynamics, and exotic attractors analysis to the (3+1)-D modified KdV–Zakharov–Kuznetsov model*, Math. Methods Appl. Sci., 2025. DOI: 10.1002/mma.70270.

[2] G. Ali, M. Marwan, U. U. Rahman and M. Hleili, *Investigation of fractional-ordered tumor–immune interaction model via fractional-order derivative*, Fractals, 2024, 32(6), 1–10.

[3] R. Ali, Z. Zhang and H. Ahmad, *Exploring soliton solutions in nonlinear spatiotemporal fractional quantum mechanics equations: An analytical study*, Opt. Quantum Electron., 2024, 56(5), 838.

[4] F. Badshah, K. U. Tariq, M. Inc and R. Javed, *On soliton solutions of Fokas dynamical model via analytical approaches*, Opt. Quantum Electron., 2024, 56(5), 743.

[5] S. Behera, *Analysis of traveling wave solutions of two space–time nonlinear fractional differential equations by the first-integral method*, Mod. Phys. Lett. B, 2024, 38(4), 2350247.

[6] S. Behera, *Multiple soliton solutions of some conformable fractional nonlinear models using Sine–Cosine method*, Opt. Quantum Electron., 2024, 56(7), 1235.

[7] J. Chen, W. Sun and S. Zheng, *Encrypting images using multiple fractional-order drive–response systems with practical finite-time synchronization*, Math. Comput. Simul., 2025, 240, 423–437.

[8] J. Chen, W. Sun and S. Zheng, *New predefined-time stability theorem and synchronization of fractional-order memristive delayed BAM neural networks*, Commun. Nonlinear Sci. Numer. Simul., 2025, 108850.

[9] Z. Eskandari, Z. Avazzadeh, R. K. Ghaziani and B. Li, *Dynamics and bifurcations of a discrete-time Lotka–Volterra model using nonstandard finite difference discretization method*, Math. Methods Appl. Sci., 2025, 48(7), 7197–7212.

[10] W. A. Faridi, M. A. Bakar, M. B. Riaz, Z. Myrzakulova, R. Myrzakulov and A. M. Mostafa, *Exploring the optical soliton solutions of Heisenberg ferromagnet-type of Akbota equation arising in surface geometry by explicit approach*, Opt. Quantum Electron., 2024, 56(6), 1046.

[11] W. A. Faridi, M. Iqbal, M. B. Riaz, S. A. AlQahtani and A.-M. Wazwaz, *The fractional soliton solutions of dynamical system arising in plasma physics: The comparative analysis*, Alexandria Eng. J., 2024, 95, 247–261.

[12] A. K. S. Hossain, M. A. Akbar and Md. I. Hossain, *Modified simple equation technique for first-extended fifth-order nonlinear equation, medium equal width equation and Caudrey–Dodd–Gibbon equation*, J. Umm Al-Qura Univ. Appl. Sci., 2024, 1–10.

[13] A. K. S. Hossain, H. Akter and M. A. Akbar, *Soliton solutions of DSW and Burgers equations by generalized (G'/G)-expansion method*, Opt. Quantum Electron., 2024, 56(4), 653.

[14] Md. N. Hossain, F. Alsharif, M. M. Miah and M. Kanan, *Abundant new optical soliton solutions to the Biswas–Milovic equation with sensitivity analysis for optimization*, Mathematics, 2024, 12(10), 1585.

[15] Md. N. Hossain, M. M. Miah, M. Alosaimi, F. Alsharif and M. Kanan, *Exploring novel soliton solutions to the time-fractional coupled Drinfel'd–Sokolov–Wilson equation in industrial engineering using two efficient techniques*, Fractal Fract., 2024, 8(6), 352.

[16] K. Hosseini, E. Hinçal, F. Alizadeh, D. Baleanu and M. S. Osman, *Bifurcation analysis, sensitivity analysis, and Jacobi elliptic function structures to a generalized nonlinear Schrödinger equation*, Int. J. Theor. Phys., 2024, 63(12), 306.

[17] Md. A. Iqbal, A. H. Ganie, Md. M. Miah and M. S. Osman, *Extracting the ultimate new soliton solutions of some nonlinear time fractional PDEs via the conformable fractional derivative*, Fractal Fract., 2024, 8(4), 210.

[18] R. Islam, M. A. Kawser, M. S. Rana and M. N. Islam, *Mathematical analysis of soliton solutions in space–time fractional Klein–Gordon model with generalized exponential rational function method*, PDEs Appl. Math., 2024, 12, 100942.

[19] Z. P. Izgi, M. O. Koprulu and H. Koçak, *Symbolic computations for exact solutions of fractional partial differential equations with reaction term*, in Computation and Modeling for Fractional Order Systems, Academic Press, 2024, 199–212.

[20] Y. Jazaa, M. Iqbal, A. R. Seadawy, S. Alqahtani, A. A. Rajhi, S. M. Boulaaras and E. A. Az-Zo'bi, *On the exploration of solitary wave structures to the nonlinear Landau–Ginsberg–Higgs equation under improved F-expansion method*, Opt. Quantum Electron., 2024, 56(7), 1181.

[21] B. Li, H. Liang and Q. He, *Multiple and generic bifurcation analysis of a discrete Hindmarsh–Rose model*, Chaos Solitons Fractals, 2021, 146, 110856.

[22] P. Li, R. Gao, C. Xu, Y. Li, A. Akgül and D. Baleanu, *Dynamics exploration for a fractional-order delayed zooplankton–phytoplankton system*, Chaos Solitons Fractals, 2023, 166, 112975.

[23] T. Mahmood, G. Alhawael, S. Akram and M. ur Rahman, *Exploring the Lie symmetries, conservation laws, bifurcation analysis and dynamical waveform patterns of diverse exact solution to the Klein–Gordon equation*, Opt. Quantum Electron., 2024, 56(12), 1978.

[24] M. A. S. Murad, W. A. Faridi, M. Iqbal, A. H. Arnous, N. A. Shah and J. D. Chung, *Analysis of Kudryashov's equation with conformable derivative via the modified Sardar sub-equation algorithm*, Results Phys., 2024, 60, 107678.

[25] M. Nadeem, F. Liu and Y. Alsayaad, *Analyzing the dynamical sensitivity and soliton solutions of time-fractional Schrödinger model with beta derivative*, Sci. Rep., 2024, 14(1), 8301.

[26] Md. M. Roshid, M. M. Rahman, H.-O. Roshid and Md. H. Bashar, *A variety of soliton solutions of time M-fractional nonlinear models via a unified technique*, PLoS One, 2024, 19(4), e0300321.

[27] A. Said, A. Bakkar, H. Khan, C. Cattani and F. Tchier, *Construction of mechanically preserved optical travelling wave solution for fractional generalized reaction Duffing model*, J. Appl. Comput. Mech., 2025.

[28] I. Samir and H. M. Ahmed, *Retrieval of solitons and other wave solutions for stochastic nonlinear Schrödinger equation with non-local nonlinearity using the improved modified extended tanh-function method*, J. Opt., 2024, 1–10.

[29] I. Samir, H. M. Ahmed, W. Rabie, W. Abbas and O. Mostafa, *Construction optical solitons of generalized nonlinear Schrödinger equation with quintuple power-law nonlinearity using Exp-function, projective Riccati, and new generalized methods*, AIMS Math., 2025, 10(2), 3392–3407.

[30] M. Shakeel, A. Bibi, A. Zafar and M. Sohail, *Solitary wave solutions of Camassa–Holm and Degasperis–Procesi equations with Atangana's conformable derivative*, Comput. Appl. Math., 2023, 42(2), 101.

[31] M. A. El-Shorbagy, S. Akram and M. ur Rahman, *Propagation of solitary wave solutions to (4+1)-dimensional Davey–Stewartson–Kadomtsev–Petviashvili equation arise in mathematical physics and stability analysis*, PDEs Appl. Math., 2024, 10, 100669.

[32] M. A. El-Shorbagy, S. Akram, M. ur Rahman and H. A. Nabwey, *Analysis of bifurcation, chaotic structures, lump and M–W-shape soliton solutions to (2+1) complex modified Korteweg–de Vries system*, AIMS Math., 2024, 9(6), 16116–16145.

[33] K. U. Tariq, M. Inc and M. S. Hashemi, *On the soliton structures to the space–time fractional generalized reaction Duffing model and its applications*, Opt. Quantum Electron., 2024, 56(4), 708.

[34] C. Xu, M. Liao, M. Farman and A. Shehzade, *Hydrogenolysis of glycerol by heterogeneous catalysis: A fractional order kinetic model with analysis*, MATCH Commun. Math. Comput. Chem., 2024, 91(3), 635–664.

[35] S. Akram and M. ur Rahman, *Multiscale soliton structures and dynamical analysis of nonlinear discrete electrical lattices modeled by the Salerno equation*, Nonlinear Dyn., 2025, 113, 32723–32744.

[36] S. Akram and Mati ur Rahman, *Exploring Nonlinear dynamics and soliton structures in the spin reduced Hirota-Maxwell-Bloch system via Atangana's conformable operator*, Chin. J. Phys., 2025, 97, 1514–1538.

[37] S. Akram, M. ur Rahman and L. A. AL-Essa, *A comprehensive dynamical analysis of (2+ 1)-dimensional nonlinear electrical transmission line model with Atangana–Baleanu derivative*, Phys. Lett. A, 2025, 130762.

[38] Y. Yasmin, H. Humaira, A. S. Alshehry, A. H. Ganie, A. M. Mahnashi and R. Shah, *Perturbed Gerdjikov–Ivanov equation: Soliton solutions via Bäcklund transformation*, Optik, 2024, 298, 171576.

[39] X. Zhang, X. Yang and Q. He, *Multi-scale systemic risk and spillover networks of commodity markets in the bullish and bearish regimes*, North Am. J. Econ. Finance, 2022, 62, 101766.

[40] X. Zhu, P. Xia, Q. He, Z. Ni and L. Ni, *Coke price prediction approach based on dense GRU and opposition-based learning salp swarm algorithm*, Int. J. Bio-Inspired Comput., 2023, 21(2), 106–121.

Received August 2025; Accepted December 2025; Available online January 2026.